Electroweakino searches at the HL-LHC in the baryon number violating MSSM

Rahool Kumar Barman,[1,2,*] Biplob Bhattacherjee,[1,†] Indrani Chakraborty[3,‡]
Arghya Choudhury,[4,§] and Najimuddin Khan[1,2,‖]

[1]*Centre for High Energy Physics, Indian Institute of Science, Bangalore 560012, India*
[2]*School of Physical Sciences, Indian Association for the Cultivation of Science, Kolkata 700032, India*
[3]*Department of Physics, Indian Institute of Technology Kanpur, Kanpur, Uttar Pradesh-208016, India*
[4]*Department of Physics, Indian Institute of Technology Patna, Bihta-801106, India*

The projected reach of direct electroweakino searches at the high luminosity LHC (HL-LHC) ($\sqrt{s} = 14$ TeV, 3000 fb^{-1} LHC) in the framework of simplified models with R-parity violating operators, $\lambda''_{112} u^c d^c s^c$ and $\lambda''_{113} u^c d^c b^c$, is studied. Four different analysis channels are chosen: Wh mediated $1l + 2b +$ jets $+ \not{E}_T$, Wh mediated $1l + 2\gamma +$ jets $+ \not{E}_T$, WZ mediated $3l +$ jets $+ \not{E}_T$ and WZ mediated $3l + 2b +$ jets $+ \not{E}_T$ and the projected exclusion/discovery reach of direct wino searches in these channels is analyzed by performing a detailed cut-based collider analysis. The projected exclusion contour reaches up to 600–700 GeV for a massless binolike χ_1^0 from searches in the Wh mediated $1l + 2b +$ jets $+ \not{E}_T$, Wh mediated $1l + 2\gamma +$ jets $+ \not{E}_T$ and WZ mediated $3l +$ jets $+ \not{E}_T$ channels, while the WZ mediated $3l + 2b +$ jets $+ \not{E}_T$ search channel is found to have a projected exclusion reach up to 600 GeV for 150 GeV $< M_{\chi_1^0} < 250$ GeV. The baryon number violating simplified scenario considered in this work is found to furnish a weaker projected reach (typically by a factor of $\sim 1/2$) than the R-parity conserving (RPC) case. The projected reach at the HL-LHC in these four channels is also recast for realistic benchmark scenarios.

I. INTRODUCTION

Supersymmetry (SUSY) [1–4] has been among the most attractive frameworks for formulating physics beyond the Standard Model (SM). Numerous studies have reported the plausibility of SUSY in resolving various inadequacies within the SM of particle physics [5–8] viz. the hierarchy problem [9,10], gauge coupling unification [11–14], existence of a viable dark matter (DM) candidate [15–17], and naturalness of Higgs mass [18,19]. In adherence to the experimental observations, SUSY has to be broken, and solution to the hierarchy problem implores the SUSY breaking scale to be $\sim O(\text{TeV})$, thus, bringing the SUSY particles within the potential reach of current and future LHC. The minimal supersymmetric extension of the Standard Model (MSSM) (see [20–24] for a detailed review) has been among the prominent class of nominees considered to address the shortcomings within the SM and in the pursuit of new physics phenomenology. A legion of studies have focused on investigating the current status and future prospects of the MSSM parameter space in light of the LHC Run-I and Run-II results [25–50]. Since the advent of the LHC, the ATLAS and CMS Collaborations have performed a multitude of searches to probe the sparticles using the LHC Run-I and Run-II dataset, however, they are yet to observe a clear signature of physics beyond the SM. Robust lower bounds have been derived on the masses of strongly interacting sparticles. Searches by the ATLAS and CMS Collaborations using the LHC $\sqrt{s} = 13$ TeV data collected at ~ 137 fb^{-1} of integrated luminosity ($\mathcal{L}$) have excluded gluinos ($\tilde{g}$) up to ~ 2.2 TeV and ~ 2.3 TeV, respectively, for a lightest SUSY particle (LSP) neutralino (χ_1^0) with mass up to ~ 600 GeV [51–53] at 95% C.L., however, within the framework of a simplified SUSY scenario. Using the same respective datasets and within a simplified scenario with some specific decay modes and mass hierarchy, ATLAS and CMS have also excluded the stops ($\tilde{t}$) and sbottoms ($\tilde{b}$) up to ~ 1.2 TeV for a $M_{\chi_1^0} \sim 400$ GeV at 95% C.L. [53–55]. On the other hand,

*rahoolbarman@iisc.ac.in
†biplob@iisc.ac.in
‡indranic@iitk.ac.in
§arghya@iitp.ac.in
‖khanphysics.123@gmail.com

the electroweakly interacting sparticles, viz. electroweakinos and sleptons, are rather feebly constrained [56–62].[1]

The MSSM is endowed with an exact symmetry related to the baryon number (B), lepton number (L) and the spin of the particle (S), referred to as R-parity (R_p).[2] R-parity conservation (RPC) entails pair production of SUSY particles at colliders and also ensures that the lightest SUSY particle, typically the χ_1^0, is stable and a viable nonbaryonic DM candidate. The presence of a stable LSP DM candidate results in missing transverse energy ($\not{E}_T$) signatures at the colliders, making the RPC scenarios extensively attractive to be analyzed at the LHC. Consequently, a myriad of studies have addressed the phenomenological implications of R-parity conserved scenarios and a nonexhaustive list of such studies can be found in [70–87].

Although the R-parity conserved scenarios display a tempting landscape for collider and astrophysical searches, it must be noted that R-parity conservation is not fundamentally necessary to obtain a viable SUSY framework. Ensuring the stability of the proton was the prime intent behind introducing R-parity conservation (relevant discussions can be found in [88,89]). However, several studies have also explored the possibility to stabilize the proton without conserving R-parity [90–93]. Another strong incentive to consider RPC scenarios is the possibility of a viable DM candidate with a correct DM relic density as discussed previously. In the presence of R-parity violation (RPV) (see [94,95] for reviews), the LSP would undergo decay and would no longer remain a viable DM candidate. However, results from [96–98] indicate that axinos and gravitinos could generate a correct relic abundance in RPV scenarios. Furthermore, the presence of R-parity violation has also been shown to ease the amount of fine-tuning required to obtain a ~125 GeV Higgs boson in SUSY [99] by weakening the bounds on gluino [100–104] and stop masses [105,106]. Another critical consequence of RPV terms is the successful explanation of the observed pattern of neutrino masses and mixing [107–113]. Within RPV scenarios, lepton number violating couplings can initiate lepton flavor violating processes (viz. the scattering of unoscillated ν_μ into τ) even in the absence of neutrino oscillation [114]. The R-parity framework has also been studied in light of offering a plausible explanation for the $(g-2)_\mu$ discrepancy [115]. In addition, the $\not{E}_T$ dependent collider search strategies, which are a trademark of RPC scenarios, would be rendered ineffective in the presence of R-parity violating terms, and the collider bounds are expected to alter. Thus, the introduction of RPV terms would result in characteristically distinct final states, a

study of which would be extremely relevant in the context of collider searches at the LHC [116,117]. Overall, the discussion until now motivates the impulse of probing the sector of RPV MSSM.

The most general, gauge invariant and renormalizable R-parity violating terms [20,118] which could be added to the MSSM superpotential ($W_{\rm MSSM}$) are the following (the notation of [119] has been followed):

$$W_{\rm RPV} = W_{\rm MSSM} + \frac{1}{2}\lambda_{ijk}L_i \cdot L_j e_k^c + \frac{1}{2}\lambda'_{ijk}L_i \cdot Q_j d_k^c$$
$$+ \frac{1}{2}\lambda''_{ijk}\epsilon_{\alpha\beta\gamma}u_i^{c\alpha}d_j^{c\beta}d_k^{c\gamma} + \mu_i H_u \cdot L_i \qquad (1.1)$$

where L and Q represent the left-handed lepton and quark superfields, respectively, while, e, u and d corresponds to the right-handed lepton, up-type quark and down-type quark superfields, respectively. λ, λ' and λ'' are the dimensionless Yukawa couplings while ϵ is the three dimensional Levi-Civita symbol. Here, i, j, k are the generation indices, α, β, γ are the flavor indices and c represents charge conjugation. The first and second terms in Eq. (1.1) violate the lepton number by 1 unit, while the third term in Eq. (1.1) violates the baryon number by 1 unit.

The collider implications of the lepton number violating RPV couplings, $\lambda_{12k}L_1 \cdot L_2 e_k^c$ ($k \in 1$, 2) and $\lambda_{i33}L_i \cdot L_3 e_3^c$ ($i \in 1$, 2), have been studied by the ATLAS Collaboration through an interpretation in simplified scenarios with winolike next-to-lightest supersymmetric particle (NLSP) pair production ($pp \to \chi_2^0/\chi_1^\pm + \chi_1^\pm$) and higgsinolike NLSP pair production ($pp \to \chi_1^0/\chi_2^0/\chi_1^\pm + \chi_1^\pm$) in the WZ and Wh mediated $4l$ [l = electrons (e) and muons (μ)] final state [120] using the LHC Run-II data collected at $\mathcal{L} = 36.1\ {\rm fb}^{-1}$. Results from [120] exclude a winolike $\chi_1^\pm$, χ_2^0 up to ~1.46 TeV (~980 GeV) for a binolike χ_1^0 with mass $M_{\chi_1^0} \sim 500\ {\rm GeV}$ ($M_{\chi_1^0} \in [400\text{--}700]\ {\rm GeV}$) in the presence of $\lambda_{12k}L_1 \cdot L_2 e_k^c$ ($\lambda_{i33}L_i \cdot L_3 e_3^c$)-type RPV coupling. The ATLAS Collaboration has also probed direct wino production in the context of RPC scenarios and has excluded winos up to ~350 GeV for a $M_{\chi_1^0} \sim 50\ {\rm GeV}$ (at 95% C.L.) from searches in the trilepton ($l = e, \mu$) + $\not{E}_T$ final state [61] using LHC Run-II data (~139 fb^{-1}). Similarly, direct wino searches by CMS in three or more charged l final states in a winolike RPC scenario, using the LHC Run-II 36 fb^{-1} dataset, have excluded winos up to ~650 GeV (WZ topology) and ~480 GeV (Wh topology) [59]. Thus, the $\frac{1}{2}\lambda_{ijk}L_i \cdot L_j e_k^c$-type RPV scenarios imply a more stringent exclusion on the electroweakino sector compared to the RPC scenarios due to harder leptons in the final state. In [121] as well, ATLAS has analyzed the four or more lepton final states in the context of RPV simplified scenario containing $\lambda_{ijk}L_i \cdot L_j e_k^c$-type couplings using the $\sqrt{s} = 8$ TeV LHC data collected at ~20.3 fb^{-1} integrated luminosity. Results from [121] exclude a

---

[1]A few phenomenological analyses in this context may be seen in Refs. [63–69].

[2]R_p is defined as $R_p = (-1)^{(3B+L+2S)}$. The SM particles and their superpartners are $R_p = +1$ and $R_p = -1$, respectively.

winolike chargino below ~750 GeV, gluino below ~1350 GeV and left-handed (right-handed) sleptons below 410) ~490 GeV GeV), for $M_{\chi_1^0} = 300$ GeV at 95% C.L., within a simplified RPV scenario where the binolike LSP χ_1^0 can decay only into electrons and muons. If the tau-rich decays are also included, the corresponding exclusion limits get weaker: winolike chargino ($\lesssim 450$ GeV), gluino ($\lesssim 950$ GeV), left-handed sleptons ($\lesssim 300$ GeV) and right-handed sleptons ($\lesssim 240$ GeV). The CMS Collaboration also analyzed the $\sqrt{s} = 8$ TeV LHC data (19.5 fb^{-1}) and excluded stops up to $\lesssim 1100$ GeV and $\lesssim 950$ GeV [122] at 95% C.L. in simplified scenarios containing λ_{122} and λ_{233}-type RPV couplings, respectively, for a binolike χ_1^0 with mass ~400 GeV. The RPV scenario with $\frac{1}{2}\lambda'_{233}L_2 \cdot Q_3 d_3^c$-type coupling has also been investigated in [122] and has excluded stops with mass between ~550 GeV and ~700 GeV for a binolike χ_1^0 with mass ~500 GeV at 95% C.L.

Gluino searches in multijet final state [123] and the jets plus two same-sign lepton or three lepton final state [124] by the ATLAS Collaboration using the LHC $\sqrt{s} = 8$ TeV data (~20 fb^{-1}) within $\lambda''_{ijk}\epsilon_{\alpha\beta\gamma}u_i^{c\alpha}d_j^{c\beta}d_k^{c\gamma}$-type RPV simplified scenario have excluded gluinos up to $\lesssim 1100$ GeV and $\lesssim 1050$ GeV, respectively, for $M_{\chi_1} \sim 400$ GeV, at 95% C.L. CMS has also searched for the gluinos in multijet [125] and same-sign dilepton plus jets final state [126] using LHC $\sqrt{s} = 8$ TeV data (~19.5 fb^{-1}) within the framework of $\lambda''_{ijk}\epsilon_{\alpha\beta\gamma}u_i^{c\alpha}d_j^{c\beta}d_k^{c\gamma}$-type RPV simplified scenarios, and have excluded gluinos below $\lesssim 650$ GeV and $\lesssim 900$ GeV, respectively, at 95% C.L. The phenomenology of $\lambda''_{ijk}u_i^c d_j^c d_k^c$-type of RPV operators has also been analyzed in [100,127] and the distinct collider signatures emerging in consequence to $\lambda'' u_i^c d_j^c d_k^c$-type of RPV coupling have been analyzed in [105,128,129]. At this point, it would be essential to take a look at the analogous exclusion limits in the RPC framework. Searches by the ATLAS and CMS Collaborations within RPC scenarios (using the LHC $\sqrt{s} = 8$ TeV, ~20 fb^{-1} dataset) have excluded gluinos up to ~1400 GeV [130] and ~1300 GeV [131], respectively, for a binolike χ_1^0 with mass ~400 GeV at 95% C.L. Using the same dataset, ATLAS and CMS also set lower limits on the mass of squarks ($\lesssim 900$ [130]) and stops ($\lesssim 760$ [132]), respectively, at 95% C.L. It is worthwhile to note that the RPC scenario and the RPV scenario discussed until now imply a comparable exclusion limit on the masses of gluinos and squarks. However, the electroweakino sector of $\lambda''_{ijk}\epsilon_{\alpha\beta\gamma}u_i^{c\alpha}d_j^{c\beta}d_k^{c\gamma}$-type RPV models still remain to be explored, and that is precisely the goal of this work.

Our aim is to study the collider constraints on electroweakinos in RPV simplified scenarios with $\lambda''_{112}u^c d^c s^c$- and $\lambda''_{113}u^c d^c b^c$-types of RPV couplings in context of searches at the future HL-LHC ($\sqrt{s} = 14$ TeV, $\mathcal{L} = 3000$ fb^{-1}). In

this analysis, we have assumed the χ_1^0 to decay promptly. The mean decay length of the LSP neutralino decaying via λ''_{ijk}-type RPV coupling is given by [95,133]

$$L(\text{cm}) = 0.3(\beta\gamma)_{\chi_1^0}\left(\frac{M_{\tilde{q}}}{100 \text{ GeV}}\right)^4\left(\frac{1 \text{ GeV}}{M_{\chi_1^0}}\right)^5\frac{3}{\lambda''_{ijk}{}^2}. \quad (1.2)$$

The consideration of a promptly decaying χ_1^0 ($L \lesssim 1$ cm) in Eq. (1.2) restricts λ''_{ijk} to values larger than $\gtrsim 10^{-4}$ and $\gtrsim 10^{-3}$ for $M_{\chi_1^0} = 30$ GeV and 10 GeV, with $M_{\tilde{q}} = 100$ GeV. Additionally, the λ''_{ijk} couplings are also bounded from above by various experimental measurements. Although our analysis is not sensitive to the value of the RPV coupling, nevertheless, it is worthwhile to discuss the existing constraints on λ''_{ijk} from various experimental measurements and theoretical limitations. Indirect upper bounds have been derived on λ''_{112} [$\lesssim 10^{-15} \times (m_{\tilde{q}}/\tilde{\Lambda} \text{ GeV})^{5/2}$, where $\tilde{\Lambda}$ is a hadronic scale and can be varied from 0.003 to 1 GeV, and $\tilde{q}$ is the squark mass] from double neutron beta decay [134]. Indirect upper limits have also been placed on λ''_{113} from neutron oscillations [135], $\lambda''_{113} \lesssim 10^{-4}$ for $m_{\tilde{q}} = 100$ GeV. This upper limit weakens to 0.002 and 0.1 for $m_{\tilde{q}} = 200$ and 600 GeV [135,136], respectively. λ''_{3jk} has been constrained from $R_l = \Gamma(Z \to$ hadronic$)/\Gamma(Z \to l\bar{l})$ to $\lesssim 0.5$ for $m_{\tilde{q}} = 100$ GeV [137,138]. At higher values of $m_{\tilde{q}}$, the theoretical bounds on λ''_{3jk} from the requirement of perturbative unification at the grand unified theory scale are more stringent. The remaining λ''_{ijk} couplings are also indirectly constrained from the perturbativity bound [95,136]. The λ''_{ijk} couplings are also constrained from the required lifetime of the LSP in order for it to be a viable candidate for dark matter. An unstable χ_1^0 LSP can also be a DM candidate provided it is abundantly long lived. Such a condition can manifest if the RPV couplings are very small. In such cases, various cosmological constraints can become relevant depending on the lifetime of the χ_1^0. For example, if the lifetime of the long-lived LSP χ_1^0 is slightly larger or comparable to the present age of the Universe, then its decay can lead to an excess of positrons or antiprotons which could lead to an incompatibility with the measurements. Resolution of this discrepancy requires that the lifetime of the χ_1^0 is sufficiently larger than the age of the Universe which in turn can be made possible only if the RPV couplings (including λ''_{ijk}) are roughly of the order of $\lesssim 10^{-20}$ [95]. The λ''_{ijk} couplings are also strongly constrained from the three-body decay of the long-lived χ_1^0: $\chi_1^0 \to e^+ + 2f$ (f = fermions) upon comparison with the observed positron flux, $\lesssim 4 \times 10^{-23}N_{1l}^{-1} \times (m_{\tilde{f}}/100\,\text{GeV})^2(m_{\chi_1^0}/100\,\text{GeV})^{-9/8}(1\,\text{GeV}/m_f)^{1/2}$ [where, N_1l ($l = 3, 4$) is the higgsino admixture in χ_1^0 and m_f is the

mass of the emitted fermion] [95]. Constraints from nucleosynthesis also impose an upper limit on the value of λ''_{ijk}. In order to remain consistent with the predictions of light nuclei abundance from big bang nucleosynthesis, the lifetime of the LSP χ^0_1, if smaller than the age of the Universe, must be within an upper limit [95]. This restriction, in turn, imposes a lower bound on the RPV couplings, $\gtrsim 10^{-12}$ [95].

Direct searches to probe λ''_{ijk} have also been performed in the context of various colliders. The work in Ref. [139] had showed that it should be possible to probe $\lambda''_{3jk} > 0.02\text{–}0.06$ for stop mass in the range of 180–325 GeV at the Run II of the Tevatron considering the stop decay: $\tilde{t}_1 \rightarrow b\chi^\pm_1 \rightarrow l\nu\chi^0_1$. The data collected by DELPHI has also been analyzed in Ref. [140] where searches for pair produced gauginos and squarks were performed and lower limits on the stop and sbottom masses ($\gtrsim 70$ GeV) were derived at 90% C.L. for various benchmark scenarios. The study in Ref. [140] considered a RPV coupling strength of $\gtrsim 10^{-3}$. Considering the stop decaying promptly into two down quarks and a sbottom, followed by a subsequent decay of the sbottom into an up and a down quark (via λ''_{ijk} coupling), the stop masses lower than 77 GeV have been excluded by OPAL [141–145]. In light of the single top quark production, various earlier studies had indicated that the LHC will play a better role in probing λ''_{ijk} among the hadron colliders [146–149]. In Ref. [149], projections have been derived on the value of $\lambda''_{ijk} \lambda''_{lmn}$ for different masses of the exchanged squarks, assuming an integrated luminosity of 30 fb^{-1} at the LHC. The CMS and ATLAS Collaborations have also performed numerous searches to probe the implications of the λ''_{lmn}-type RPV couplings and have derived exclusion limits on sparticle masses. The ATLAS Collaboration has performed a search in the multiple b-jet final state produced from the cascade decay of direct produced lightest stop pair using the LHC Run-II data collected at $\mathcal{L} \sim 139$ fb^{-1} [150]. The light stops are assumed to decay into a higgsinolike $\chi^\pm_1$ and a top quark or a χ^0_1/χ^0_2 and a bottom quark. The $\chi^\pm_1, \chi^0_1$ and the χ^0_2 are considered to be mass degenerate and they have been assumed to undergo decay via $\chi^\pm_1 \rightarrow bbs$ and $\chi^0_2/\chi^0_1 \rightarrow tbs$ (on account of the λ''_{323} RPV coupling). The analysis in Ref. [150] considers λ''_{323} in the order of $\sim O(10^{-2}\text{–}10^1)$ which ensures promptly decaying charginos and neutralinos, and has excluded light stops with masses up to ~ 950 GeV in the $m_{\tilde{t}} \le m_t + m_{\chi^0_2,\chi^0_1,\chi^\pm_1}$ region at 95% C.L. Reference [151] utilizes the LHC Run-II data collected at $\mathcal{L} \sim 36$ fb^{-1} to search for LSP stops decaying into two jets via the λ''_{ijk} couplings, and excludes stop mass in the range of 100–400 GeV at 95% C.L. for stop decaying into two light flavored jets. The stop mass ranges, 100–470 GeV and 480–610 GeV, are excluded at 95% C.L., when the stop decays into a b jet and a light jet. The CMS Collaboration has also used the same dataset to

search for pair produced stops [152], each decaying to a pair of quarks via the λ''_{ijk} couplings. The study in Ref. [152], in particular, has considered two different RPV coupling scenarios, $\tilde{t} \rightarrow qq'$ (via λ''_{312}) and $\tilde{t} \rightarrow bq'$ (via λ''_{323}), and has considered a relatively large RPV coupling such that the stops undergo prompt decay. This search has excluded stop masses in the range of 80–520 GeV with the λ''_{312}-type RPV couplings and 80–270 GeV, 285–340 GeV, 400–525 GeV, with the λ''_{323}-type RPV couplings, at 95% C.L. We conclude the ongoing summarized revisit section by making a comment on the intermediate case, where the decay length of LSP is neither too large nor zero, i.e., where the decay vertex of the mother particle is displaced. The minimum distance between the production and decay vertex for differentiating them experimentally is $\mathcal{O}(2 \times 10^{-5}$ m); from Eq. (1.2) the upper limit on the RPV coupling reads

$$\lambda''_{ijk} < \sqrt{3} \times 1.2 \times 10^{-4} \gamma^{\frac{1}{2}} \left(\frac{M_{\tilde{f}}}{100 \text{ GeV}} \right)^2 \left(\frac{100 \text{ GeV}}{M_{\tilde{\chi}^0_1}} \right)^{\frac{5}{2}},$$

(1.3)

with γ being Lorentz boost factor. Thus the long-lived LSP might be probed through the detection of displaced vertices as well if the couplings lie within the window of $\mathcal{O}(10^{-5}\text{–}10^{-4})$ [95].

A $\lambda''_{ijk}u^c_i d^c_j d^c_k$-type of RPV scenario, where the LSP would decay into a multijet final state, $\chi^0_1 \rightarrow j_u j_d j_d$ ($j_u = u, c, t$ and $j_d = d, s, b$), would be expected to be amply sensitive to search strategies which consider large jet multiplicity in the final state. However, if the jets produced from the decay of χ^0_1 are highly collimated, then they would evade identification as isolated jets, thereby, altering the reach of collider search strategies. Within simplified RPC scenarios, direct wino searches in the Wh mediated $1l + 2b + \not{E}_T$ and WZ mediated $3l + \not{E}_T$ ($l = e, \mu$) final states [153] furnish robust bounds on the mass of winos as a function of $M_{\chi^0_1}$. In this work, we analyze these collider searches in the context of $\lambda''_{112}u^c d^c s^c$-type RPV simplified scenarios[3] (in Sec. II A and Sec. II C, respectively) and contrast them with the results for RPC scenarios in [153]. Additionally, we also explore the future reach of direct wino searches in the Wh mediated $1l + 2\gamma + \text{jets} + \not{E}_T$ final state (Sec. II B) and WZ mediated $3l + 2b + \text{jets} + \not{E}_T$ final state (Sec. II D), respectively characterized by $\lambda''_{112}u^c d^c s^c$- and $\lambda''_{113}u^c d^c b^c$-type of RPV operators. We have considered final states containing leptons/photons in addition to the multiple jets since they are easier to trigger and offer a cleaner signature. A few benchmark scenarios and their collider implications are discussed in Sec. III. We conclude in Sec. IV.

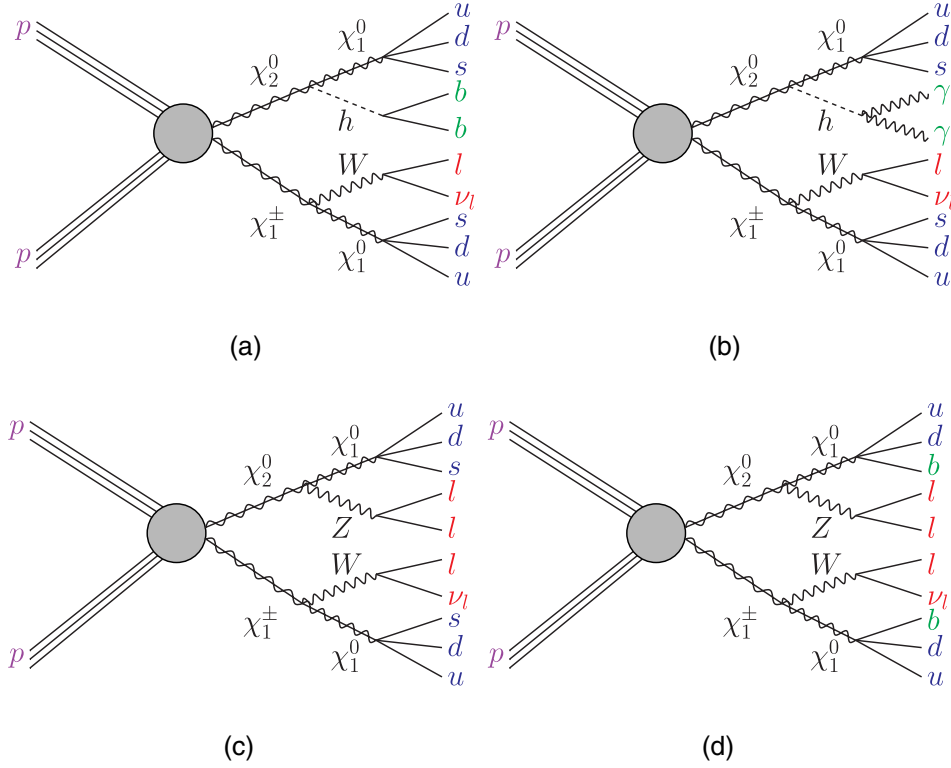[3]The respective final states feature additional light jets produced from the decay of χ^0_1.

FIG. 1. Feynman diagrams representing the cascade decay chain of $\chi_2^0 \chi_1^\pm$ pair into (a) Wh mediated $1l + 2b + \text{jets} + \not{E}_T$, (b) Wh mediated $1l + 2\gamma + \text{jets} + \not{E}_T$, (c) WZ mediated $3l + \text{jets} + \not{E}_T$ and (d) WZ mediated $3l + 2b + \text{jets} + \not{E}_T$ final state. Here, jets represents the light quark jets, while l corresponds to an electron or muon.

II. COLLIDER ANALYSIS

A simplified SUSY scenario [154] with mass degenerate winolike χ_2^0, $\chi_1^\pm$, and a binolike χ_1^0 is considered in this analysis. We consider the direct production of winolike $\chi_2^0 \chi_1^\pm$ pair due to its higher production cross section compared to wino-type neutralino pair ($\chi_2^0 \chi_2^0$) or chargino pair ($\chi_1^\pm \chi_1^\mp$). Furthermore, the wino production cross section is also roughly ~2 times larger than the higgsino production rates. Correspondingly, the other SUSY particles namely sleptons, squarks, heavy Higgses and the heavier electroweakinos (χ_3^0, χ_4^0, $\chi_2^\pm$) have been fixed at a higher mass in order to decouple their effects on our study.

Direct wino pair production is considered ($pp \to \chi_2^0 \chi_1^\pm$) and a detailed collider analysis is performed in multifarious final states originating from the cascade decay of the aforesaid $\chi_2^0 \chi_1^\pm$ pair. As stated in Sec. I, our aim is to study the collider ramifications of the baryon number violating RPV operator in simplified MSSM. To reiterate the structure of this paper, we study the implications of $\lambda''_{112} u^c d^c s^c$-type RPV term in Secs. II A, II B and II C and $\lambda''_{113} u^c d^c b^c$-type RPV term in Sec. II D. In light of these terms, the χ_1^0 decays into a *uds* final state in the initial three cases while the χ_1^0 decays into a *udb* final state in the latter case, resulting in final states with large jet multiplicity. The Feynman diagrams of the signal processes considered in

Secs. II A, II B, II C and II D have been illustrated in Figs. 1(a), 1(b), 1(c) and 1(d), respectively.

In the present work, the signal events have been generated using PYTHIA-6.4.28 [155,156], while the MadGraph_aMC@NLO [157] framework has been used to generate the background events at leading order (LO) parton level in SM. Subsequent showering and hadronization has been performed through PYTHIA-6.4.28. The background events have been generated by matching up to 3 jets (the 3 jet matched sample of a background process bkg will be represented as bkg + jets) except for the $W/Z + \text{jets}$ background process for which the 4 jet matched sample is used. The fast detector response has been simulated using DELPHES-3.4.1 [158]. The default ATLAS configuration card which comes along with DELPHES-3.4.1 package has been used in the entirety of this analysis.[4] For the background processes, we have considered the leading order (LO) cross sections computed by MadGraph_aMC@NLO unless stated otherwise. The next-to-leading order + next-to-leading logarithmic (NLO-NLL) order cross sections (taken from [159,160]) have been considered for the signal processes (direct wino production: $\sigma^{\text{wino}}_{pp \to \chi_2^0 \chi_1^\pm}$).

---

[4]The b-jet tagging efficiency has been assumed to be 70% while the $c \to b$ ($u, d, s \to b$) mistag efficiency has been assumed to be 30% (1%).

In the following subsections, we present a detailed discussion of the collider search strategy employed to maximize the signal significance in the corresponding search channels and present our results on the projected reach of direct wino searches in these respective search channels at the HL-LHC.

A. Searches in Wh mediated $1l + 2b + \text{jets}(N_j \geq 2) + \not{E}_T$ channel

The signal process considered in this subsection is illustrated in Fig. 1(a). The $\chi_1^\pm$ and χ_2^0 are assumed to decay into $W\chi_1^0$ and $h\chi_1^0$, respectively, with a branching ratio of 100%, while, the SM branching values for $h \to b\bar{b}$ ($\sim$57% [161]) and $W \to l'\nu$ ($\sim$31.7% [161], $l' = e, \mu, \tau$) have been considered. The cascade decay process culminates in two χ_1^0 along with other SM particles. The RPV operator $\lambda_{112}'' u^c d^c s^c$ implies $\chi_1^0 \to uds$, resulting in multiple light quark jets in the final state. The cascade decay chain eventually results in Wh mediated $1l + 2b + \text{jets} + \not{E}_T$ final state.

An event is required to have exactly one isolated lepton ($l = e, \mu$), at least two light jets ($N_j \geq 2$), and exactly two b jets in the final state. The electron (muon) is considered to be isolated if $\Sigma p_T^{\text{others}}/p_T^l$ is ≤ 0.12 for electrons and ≤ 0.25 for muons, where $\Sigma p_T^{\text{others}}$ is the scalar sum of transverse momenta of charged particles with $p_T \geq 0.5$ GeV (excluding the lepton under consideration) within a cone of radius $\Delta R = 0.5$ centered around the direction of lepton momentum and p_T^l is the transverse momentum of the lepton. Here, ΔR is defined as $\Delta R = \sqrt{\Delta\eta^2 + \Delta\phi^2}$, where $\Delta\eta$ and $\Delta\phi$ are the differences in pseudorapidity and the azimuthal angle, respectively, between the lepton under consideration and the charged particle. The isolated electron (muon) is required to have $p_T > 30$ GeV, while the lighter jets and the b jets are required to have $p_T > 20$ GeV. In addition, the final state leptons and quarks must lie within a pseudorapidity range of $\leq |2.5|$.

The most dominant source of background is $t\bar{t} + \text{jets}$. Contributions to the background also arise from $WZ + \text{jets}$, $WW + \text{jets}$ and $ZZ + \text{jets}$ when W, Z undergoes decay via leptonic decay modes. Additional contributions arise from $Wh + \text{jets}$ and $Zh + \text{jets}$ when the h decays to $b\bar{b}$ while the W/Z decays leptonically. Contributions from $Wb\bar{b} + \text{jets}$, $Wc\bar{c} + \text{jets}$ (here, the c jet get mistagged as a b jet) and $W + \text{jets}$ are also considered. Here, we have considered the NLO cross section for $t\bar{t} + \text{jets}$, where the NLO cross section has been computed by multiplying the NLO k factor ($k = 1.5$) with the LO cross section obtained from MadGraph_aMC@NLO. The cross section of background processes has been listed in the Appendix (see Table VIII).

Signal events have been generated for various combinations of $M_{\chi_2^0}(= M_{\chi_1^\pm})$ and $M_{\chi_1^0}$. $M_{\chi_2^0}$ has been varied from 200 GeV to 1 TeV with a step size of 25 GeV, while $M_{\chi_1^0}$

has been varied between 25 GeV to $M_{\chi_2^0} - 125$ GeV with a step size of 10 GeV. Three different signal regions are chosen, SR1-A, SR1-B and SR1-C, aimed at maximizing the significance of signal events with small, intermediate and large mass difference, respectively, between the NLSP $\chi_2^0, \chi_1^\pm$ and LSP χ_1^0. The selection cuts for SR1-A, SR1-B and SR1-C have been chosen by performing a cut-based analysis for the three representative benchmark points: BP1-A: $M_{\chi_2^0} = 200$ GeV, $M_{\chi_1^0} = 55$ GeV, BP1-B: $M_{\chi_2^0} = 350$ GeV, $M_{\chi_1^0} = 165$ GeV and BP1-C: $M_{\chi_2^0} = 500$ GeV, $M_{\chi_1^0} = 25$ GeV, respectively. The values of $\sigma_{pp \to \chi_2^0 \chi_1^\pm}^{\text{wino}}$ for BP1-A, BP1-B and BP1-C have been listed in the Appendix. The signal yield (S) has been computed as follows:

$$S = \sigma_{pp \to \chi_2^0 \chi_1^\pm}^{\text{wino}} \times \mathcal{L} \times \text{Eff}$$
$$\times \text{Br}(\chi_2^0 \chi_1^\pm \to W\chi_1^0 h\chi_1^0 \to l\nu b\bar{b} + \text{jets}) \quad (2.1)$$

where $\mathcal{L}$ is the integrated luminosity ($\mathcal{L} = 3000$ fb^{-1} for HL-LHC) and Eff. represents the efficiency of the signal region.[5]

A variety of kinematic variables have been used to design the optimized signal regions. First and foremost, the invariant mass of the two final state b jets, $M_{b_1 b_2}$ (b_1 and b_2 represents the p_T ordered leading and subleading b jets in the final state), is used to discriminate the background. For the signal process, the $b\bar{b}$ pair is produced from the decay of the h and thereby peaks roughly around $\sim$110–115 GeV. On the other hand, the $M_{b_1 b_2}$ distribution for the most dominant $t\bar{t} + \text{jets}$ background has a smoothly falling distribution since the two b jets are produced from the decay of two different top quarks. The $M_{b_1 b_2}$ distribution for the signal benchmark points and the $t\bar{t} + \text{jets}$ background has been shown in Fig. 2(a).[6] The distributions for BP1-A, BP1-B and BP1-C in Fig. 2 have been illustrated as red, blue and purple solid colors while the $t\bar{t} + \text{jets}$ background has been shown in brown color.

The $t\bar{t} + \text{jets}$ background also undergoes a considerable reduction upon the application of a lower bound on the contransverse mass (M_{CT}) [162,163], where M_{CT} is defined as $M_{\text{CT}} = \sqrt{(E_T^{b1} + E_T^{b2})^2 - |\vec{p_T}^{b1} - \vec{p_T}^{b2}|^2}$. Here, $\vec{p_T}^{bi}$ and E_T^{bi} are transverse momentum and energy of the ith b jet. The normalized M_{CT} distribution for the signal benchmark points and the $t\bar{t} + \text{jets}$ background has been shown in Fig. 2(b).

---

[5]Eff. is the ratio of the number of signal events which pass through a certain signal region (IEV) to the total number of generated signal events (NEV); Eff = $\frac{\text{IEV}}{\text{NEV}}$.

[6]The cross section for $t\bar{t} + \text{jets}$ process is roughly an order of magnitude higher than the other relevant backgrounds, and, therefore, for the sake of illustrative clarity, we display the kinematic distribution for the $t\bar{t} + \text{jets}$ background process only in Fig. 2.
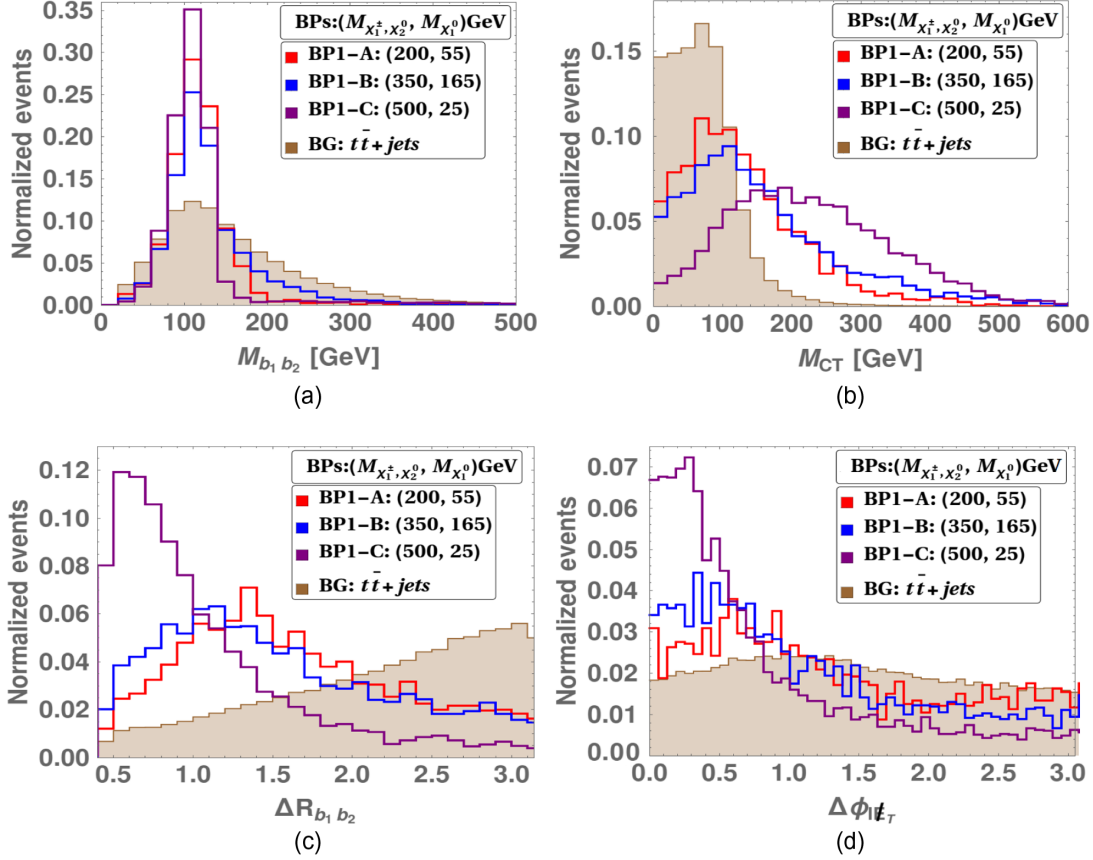
FIG. 2. Normalized distributions of $M_{b_1 b_2}$ (a), M_{CT} (b), $\Delta R_{b_1 b_2}$ (c), $\Delta \Phi_{l \ell_T}$ (d) are shown for BP1-A (red solid line), BP1-B (blue solid line), BP1-C (purple solid line) and the $t\bar{t}$ + jets background (brown color).

The invariant mass of the first three p_T ordered light jets, $M_{j_1 j_2 j_3}$, and the scalar sum of their transverse momenta, H_T, are also utilized in performing the cut-based analysis. The larger mass difference (ΔM) between ($\chi_2^0, \chi_1^\pm$) and χ_1^0 in BP1-C results in the χ_1^0 being produced with a relatively larger boost, thereby producing more collimated light jets from the decay of χ_1^0. As a result, the kinematic variables constructed by using the momenta of the leading light jets (H_T and $M_{j_1 j_2 j_3}$) peak at a higher value for signal scenarios with large mass difference between the NLSP and the LSP (viz. BP1-C) as compared to the cases where the χ_2^0 and χ_1^0 are closer in mass to each other (viz. BP1-B and BP1-A).

In addition, the ΔR between the two final state b jets, $\Delta R_{b_1 b_2}$, and the difference between the azimuthal angles of the final state lepton and the $\slashed{E}_T$, $\Delta \phi_{\ell, \slashed{E}_T}$, are also used in constructing the optimized signal regions. The three benchmark points, BP1-A, BP1-B and BP1-C, feature an on-shell h produced from the decay of $\chi_2^0 \to \chi_1^0 h$. For the case of BP1-C, the relatively larger ΔM between χ_2^0 and χ_1^0 results in a h with relatively larger boost as compared to the case of BP1-A and BP1-B. Thereby, the $b\bar{b}$ pair in the final state of BP1-C is more collimated. As a result, $\Delta R_{b_1 b_2}$ in BP1-C peaks at a smaller value ($\Delta R_{b_1 b_2} \sim 0.7$) than in BP1-B

($\Delta R_{b_1 b_2} \sim 1.4$). Similarly, the $\Delta R_{b_1 b_2}$ distribution for BP1-B peaks at a relatively lower value (at $\Delta R_{b_1 b_2} \sim 1.1$) than for BP1-A. Furthermore, the $b\bar{b}$ pair which originates from the $t\bar{t}$ + jets background is generated from two different mother particles, and therefore, are widely separated in the azimuthal angle. Consequently, $\Delta R_{b_1 b_2}$ for the $t\bar{t}$ + jets background peaks at further larger values ($\Delta R_{b_1 b_2} \sim 3$). The normalized $\Delta R_{b_1 b_2}$ distribution has been illustrated in Fig. 2(c), where the red, blue and purple solid lines represents BP1-A, BP1-B and BP1-C, respectively, while the brown colored region represents the $t\bar{t}$ + jets background. Additionally, we also consider the azimuthal angular separation between the l (produced from $W \to l\nu$) and $\slashed{E}_T$, represented as $\Delta \phi_{\ell, \slashed{E}_T}$, in performing the cut-based analysis. For BP1-C, $\Delta \phi_{\ell, \slashed{E}_T}$ peaks at a lower value than in BP1-B/BP1-A. The normalized distributions of $\Delta \phi_{\ell, \slashed{E}_T}$ for BP1-A, BP1-B, BP1-C and $t\bar{t}$ + jets have been shown in Fig. 2(d).

It is to be noted that the top quark dominantly decays into a bW pair and effectively contributes to the background when one of the W boson undergoes leptonic decay while the other W decays hadronically. One obtains two solutions for the z component of momentum of the neutrino (p_z^ν) produced from the leptonically decaying

TABLE I. Selection cuts corresponding to SR1-A, SR1-B and SR1-C, optimized to maximize the signal significance of signal processes with small, intermediate and large ΔM between the NLSP $\chi_1^{\pm}, \chi_2^0$ and the LSP χ_1^0, respectively, for searches in the Wh mediated $1l + 2b + \text{jets} + \not{E}_T$ channel at the HL-LHC, are shown. The cut flow table for BP1-A, BP1-B and BP1-C and the relevant backgrounds are also tabulated along with the respective signal significance values.

SR1-A

Cut variables		$M_{b_1 b_2}$	$M_{\rm CT}$	$\Delta R_{b_1 b_2}$	$\Delta\phi_{l,\not{E}_T}$	$M_{l\not{E}_T b}$	$\cdots$	$\cdots$
		(GeV)	(GeV)			(GeV)	$\cdots$	$\cdots$
Selection cuts for SR1-A		70–130	>200	<1	<1.25	>190	$\cdots$	$\cdots$
	Signal (BP1-A)	4.54×10^4	5823	4881	3311	2655	$\cdots$	$\cdots$
	$t\bar{t}$ + jets	2.78×10^7	5.35×10^5	4.80×10^5	3.01×10^5	2.01×10^5	$\cdots$	$\cdots$
	WZ + jets	4.38×10^4	7211	7211	4635	3708	$\cdots$	$\cdots$
Signal and background yields	WW + jets	1.41×10^4	1393	1393	806	440	$\cdots$	$\cdots$
	ZZ + jets	6064	683	668	282	222	$\cdots$	$\cdots$
	Wh + jets	5595	859	676	553	417	$\cdots$	$\cdots$
	Zh + jets	1249	129	51	38	23	$\cdots$	$\cdots$

Total background yield: 2.05×10^5 Total signal yield: 2655   Signal significance: 5.9

SR1-B

Cut variables		$M_{b_1 b_2}$ (GeV)	$M_{\rm CT}$ (GeV)	$M_{j_1 j_2 j_3}$ (GeV)	H_T (GeV)	$\Delta R_{b_1 b_2}$	$\Delta\phi_{l,\not{E}_T}$	$M_{l\not{E}_T b}$ (GeV)
Selection cuts for SR1-B		70–130	>160	>140	>210	<1	<1	>200
90 Signal and background yields	Signal (BP1-B)	6975	2317	2228	1999	1277	729	572
	$t\bar{t}$ + jets	2.79×10^7	1.22×10^6	9.37×10^5	6.92×10^5	4.63×10^5	1.88×10^5	7.75×10^4
	WZ + jets	4.38×10^4	1.24×10^4	8447	7313	6799	3914	2575
	WW + jets	1.41×10^4	2199	1906	1686	1466	586	293
	ZZ + jets	6063	1293	907	743	684	193	134
	Wh + jets	5595	859	631	602	334	209	129
	Zh + jets	1249	130	45	43	28	21	6.4

Total background yield: 8.07×10^4 Total signal yield: 572   Signal significance: 2.0

SR1-C

Selection cuts for SR1-C		70–130	>160	>140	>240	<1	<1	>360
	Signal (BP1-C)	3147	2168	2061	1950	1672	1206	464
	$t\bar{t}$ + jets	2.79×10^7	1.22×10^6	9.37×10^5	6.01×10^5	4.03×10^5	1.63×10^5	1.06×10^4
	WZ + jets	4.39×10^4	1.24×10^4	8447	6696	6181	3708	515
Signal and background yields	WW + jets	1.4148×10^4	2199	1906	1393	1173	440	73.3
	ZZ + jets	6063	1292	907	624	580	178	0.0
	Wh + jets	5595	859	631	602	334	188	32
	Zh + jets	1249	130	45	42	28	19	0.4

Total background yield: 1.13×10^4 Total signal yield: 464   Signal significance: 4.4

W: $p_z^{\nu} = (a_1 p_z^l \pm \sqrt{a_3})/a_2$, were $a_1 = p_x^l \not{E}_x + p_y^l \not{E}_y + \frac{M_W^2}{2}$, $a_2 = E^{l2} - p_z^{l2}$ and $a_3 = E^{l2} a_1^2 - a_2 E^{l2} (\not{E}_x^2 + \not{E}_y^2)$, with $p_{x,y,z}^l$ representing the x, y, z components of momentum of the lepton, E^l representing the energy of the lepton, and $\not{E}_{x,y}$ represents the x component and y component of the missing transverse energy. The signal process considered in the current analysis contains two b jets in the final state, and, coupled with the two possible solutions for p_z^{ν}, results in two different values of $M_{l\not{E}_T b_1}$ ($j = 1, 2$) and two values of $M_{l\not{E}_T b_2}$. Here, $M_{l\not{E}_T b_i}$ ($i = 1, 2$) represents the invariant mass of the final state lepton, the missing energy and the b jets. The $M_{l\not{E}_T b_i}$ variable is effective against the $t\bar{t}$ + jets background where the only contribution to $\not{E}_T$ comes from the ν produced by the leptonically decaying W. In this regard, we compute all four values of $M_{l\not{E}_T b_i}$ and choose the combination whose value is closest to the top mass. The invariant mass of the aforesaid combination is represented as $M_{l\not{E}_T b}$ and has been used in performing the cut-based analysis.
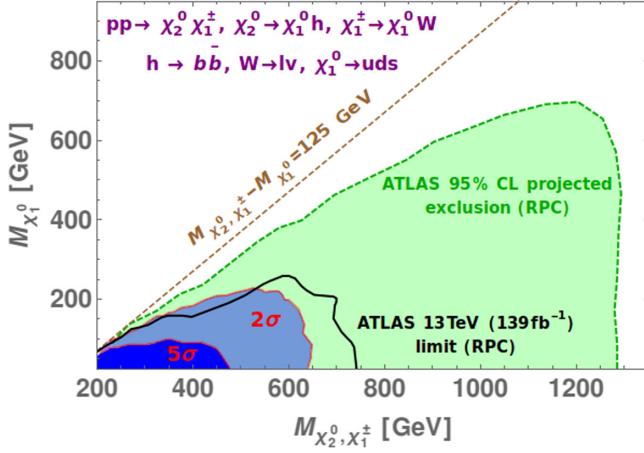
FIG. 3. The projected discovery and exclusion regions are shown in dark blue and light blue colors, respectively, in the $M_{\chi_1^0} - M_{\chi_2^0, \chi_1^\pm}$ plane. The projection contours have been derived from searches in the $1l + 2b + \text{jets} + \not{E}_T$ final state resulting from the cascade decay of directly produced winolike $\chi_2^0 \chi_1^\pm$ pair within a simplified model scenario containing $\lambda''_{112} u^c d^c s^c$-type RPV term, at the HL-LHC ($\sqrt{s} = 14$ TeV, $\mathcal{L} \sim 3$ ab^{-1}). The solid black line represents the current observed limit at 95% C.L. from direct wino searches in the WH mediated $1l + 2b + \not{E}_T$ final state, in a RPC simplified scenario, derived by ATLAS using the LHC Run-II dataset collected at $\mathcal{L} \sim 139$ fb^{-1} [62]. The light green colored region corresponds to the projected exclusion reach (at 95% C.L.) of HL-LHC, derived by ATLAS, in direct wino searches in the WH mediated $1l + 2b + \not{E}_T$ final state within a simplified RPC scenario [153]. The brown dashed line represents the condition for on-shell Higgs production ($M_{\chi_2^0, \chi_1^\pm} - M_{\chi_1^0} = 125$ GeV).

The optimized selection cuts corresponding to SR1-A, SR1-B and SR1-C have been shown in Table I. The signal yields for BP1-A, BP1-B and BP1-C, along with the corresponding background yields obtained after successive application of selection cuts listed in SR1-A, SR1-B and SR1-C, respectively, have also been shown in Table I. It should be noted that the signal significances[7] tabulated in Table I have been obtained without assuming any systematic uncertainty. SR1-A results in a signal significance of 5.9 for BP1-A, while SR1-B and SR1-C have a signal significance of 2.0 and 4.4 for BP1-B and BP1-C, respectively.

We also derive the projected exclusion limits in the $M_{\chi_1^0} - M_{\chi_2^0, \chi_1^\pm}$ plane from direct wino searches at the HL-LHC in the Wh mediated $1l + 2b + \text{jets} + \not{E}_T$ search channel. The value of signal significance is computed for the three optimized signal regions and the maximum among them is considered in deriving the projection regions.[8] The projected exclusion and discovery region

---

[7]The signal significance is computed as $S/\sqrt{B}$, where S and B are the signal and background yields.

[8]The same strategy has been followed in all the analyses considered in this work.

corresponds to the sector with signal significance $> 2\sigma$ and $> 5\sigma$, respectively. They have been represented in light blue and dark blue colors, respectively, in Fig. 3. The brown dashed line in the same figure corresponds to the on-shell mass condition for h production and represents the mass correlation: $M_{\chi_2^0} - M_{\chi_1^0} = 125$ GeV. It can be observed from Fig. 3 that within the framework of a $\lambda''_{112} u^c d^c s^s$-type RPV simplified scenario, direct wino searches at the HL-LHC in the Wh mediated $1l + 2b + \text{jets} + \not{E}_T$ search channel have a potential exclusion (discovery) reach up to $\sim$630 GeV ($\sim$450 GeV) for a binolike $M_{\chi_1^0} \sim 0$ GeV.

The ATLAS Collaboration has also analyzed the current observed limit ($\sqrt{s} = 13$ TeV, $\mathcal{L} = 139$ fb^{-1}) as well as the projected reach of direct wino production at the HL-LHC in the analogous channel for the RPC scenario: Wh mediated $1l + 2b + \not{E}_T$ final state in [62,153], respectively. The current observed limit (at 95% C.L.) reaches up to $M_{\chi_2^0, \chi_1^\pm} \sim$ 720 GeV for $M_{\chi_1^0} = 100$ GeV. The projected exclusion and discovery contour of ATLAS reaches up to $M_{\chi_2^0, \chi_1^\pm} \sim$ 1300 GeV and $\sim$600 GeV for a binolike χ_1^0 with mass up to 100 GeV at 95% C.L. The ATLAS exclusion contour has been shown in light green color in Fig. 3. Thus, the projected reach of direct wino searches interpreted in a RPC simplified scenario can get significantly weakened in the presence of $\lambda''_{112} u^c d^c s^c$-type RPV coupling. In the next three subsections, we further study the collider implications of RPV couplings in different final states.

B. Searches in Wh mediated $1l + 2\gamma + \text{jets}(N_j \geq 2) + \not{E}_T$ channel

In the current subsection, we consider the process: $pp \rightarrow \chi_1^\pm \chi_2^0 \rightarrow (W\chi_1^0)(h\chi_1^0) \rightarrow (l\nu uds)(\gamma\gamma uds)$, which culminates in $1l + 2\gamma + \text{jets} + \not{E}_T$ final state [Fig. 1(b)]. Here, $\text{Br}(\chi_1^\pm \rightarrow W\chi_1^0)$ and $\text{Br}(\chi_2^0 \rightarrow h\chi_1^0)$, have been assumed to be 100%. The small branching rate of $h \rightarrow \gamma\gamma$ is a significant drawback for this channel, however, a large photon detection efficiency, sharp diphoton invariant mass peak and a smaller background make it a promising one. Unlike the Wh mediated $1l + 2b + \text{jets} + \not{E}_T$ channel (discussed in Sec. II A), no HL-LHC projection study has been performed for the analogous RPC scenario channel (Wh mediated $1l + 2\gamma + \not{E}_T$).

The event selection criteria requires the presence of exactly one isolated lepton ($l = e, \mu$), two photons, and at least two light jets ($N_j > 2$) in the final state. The lepton isolation criteria specified in Sec. II A is implemented here as well. The final state lepton, jets and photons satisfy the criteria: $|\eta^{l, \text{jet}, \gamma}| < 2.5$ and $p_T^{l, \text{jet}, \gamma} > 30, 30, 20$ GeV respectively. In addition, we demand that no pair of final state particles must be within $\Delta R < 0.5$ of each other. Furthermore, a b-jet veto is applied.

The most dominant contribution to the background comes from the $t\bar{t}h + \text{jets}$ and $Wh + \text{jets}$ processes.
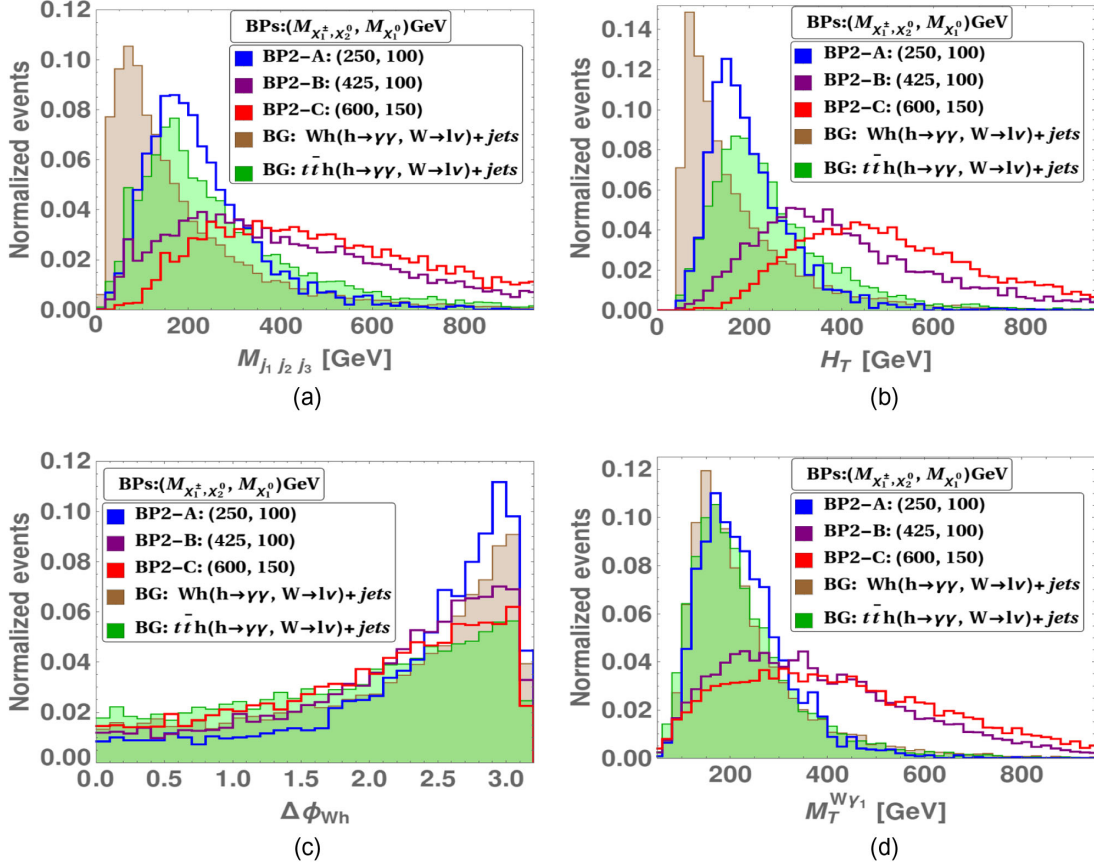
FIG. 4. Normalized distribution of $M_{j_1 j_2 j_3}$ (a), H_T (b), $\Delta\phi_{Wh}$ (c) and $M_T^{W\gamma_1}$ (d) are shown for BP2-A (blue solid line), BP2-B (purple solid line), BP2-C (red solid line). The corresponding distributions for $t\bar{t}h$ + jets and Wh + jets are also shown in brown and green colored regions.

Subdominant contribution to the background arises from Zh + jets and W/Z + jets.[9]

The signal events have been generated by varying $M_{\chi_2^0}(= M_{\chi_1^\pm})$ in between 200 GeV to 1000 GeV with a step size of 25 GeV, while $M_{\chi_1^0}$ has been varied between 25 GeV to $M_{\chi_2^0,\chi_1^\pm} - 125$ GeV, with a step size of 25 GeV. We choose three representative benchmark points, BP2-A: $M_{\chi_2^0} = 250$ GeV, $M_{\chi_1^0} = 100$ GeV (small ΔM), BP2-B: $M_{\chi_2^0} = 425$ GeV, $M_{\chi_1^0} = 100$ GeV (intermediate ΔM), and BP2-C: $M_{\chi_2^0} = 600$ GeV, $M_{\chi_1^0} = 150$ GeV (large ΔM), and perform a cut-based collider analysis. The cross-section values for the background processes and the signal benchmark points have been listed in the Appendix.

The kinematic variables used to perform the cut-based analysis are $M_{\gamma\gamma}$ (invariant mass of the di-photon pair), $M_{j_1 j_2 j_3}$ (invariant mass of the three leading jets), H_T (scalar sum of transverse momenta of the three leading jets), $\Delta\phi_{Wh}$

[difference in the azimuthal angle of the lepton-$\not{E}_T$ system and the $\gamma\gamma$ system (originated from h)] and the transverse mass of the $W\gamma_i$ system, $M_T^{W\gamma_i}$ ($i = 1, 2$). Here $M_T^{W\gamma_i}$ ($i = 1, 2$) is defined as $M_T^{W\gamma_i} = \sqrt{(M_T^W)^2 + 2E_T^W E_T^{\gamma_i} - 2\vec{p}_T^W \vec{p}_T^{\gamma_i}}$. M_T^W, E_T^W ($= \sqrt{M_W^2 + |\vec{p}_T^W|^2}$) and $\vec{p}_T^W$ are the transverse mass, energy and momentum of the leptonically decaying W boson, respectively. $E_T^{\gamma_i}$ and $\vec{p}_T^{\gamma_i}$ are the transverse energy and momentum of the ith photon.

The normalized distributions of $M_{j_1 j_2 j_3}$, H_T, $\Delta\phi_{Wh}$ and $M_T^{W\gamma_1}$ for BP2-A (blue solid line), BP2-B (purple solid line) and BP2-C (red solid line), are represented in Figs. 4(a), 4(b), 4(c) and 4(d), respectively. The normalized distributions of the dominant background processes, $t\bar{t}h$ + jets and Wh + jets, are also shown as brown and green colored regions, respectively. Considering the high reconstruction and identification capability of the photons at the LHC, we restrict $M_{\gamma\gamma}$ to a narrow range around m_h: 122 GeV $\leq M_{\gamma\gamma} \leq$ 128 GeV. The cut on $M_{\gamma\gamma}$ effectively diminishes the contribution from the W/Z + jets background. The other kinematic variables, $M_{j_1 j_2 j_3}$, H_T and M_T^W, help in suppressing the contributions from the other background processes, all of which contain an h.

---

[9]The W/Z + jets process contributes to the background of the $1l + 2\gamma$ + jets + $\not{E}_T$ signal when the W/Z decays leptonically and jets get faked as photons. In the present analysis, we have assumed a jet $\rightarrow \gamma$ fake rate of 0.05% [164].

TABLE II. The selection cuts corresponding to the signal regions, SR2-A, SR2-B and SR2-C designed to maximize the signal significance of BP2-A, BP2-B and BP2-C, respectively, for searches in the Wh mediated $1l + 2\gamma + \text{jets} + \not{E}_T$ channel, are listed. The cut flow table for BP2-A, BP2-B, BP2-C and other relevant backgrounds is also tabulated. The signal significance values have also been listed.

		$M_{\gamma\gamma}$ (GeV)	$M_{j_1 j_2 j_3}$ (GeV)	H_T (GeV)	$\Delta\phi_{Wh}$	$M_T^{W\gamma_1}$ (GeV)
		SR2-A				
Cut variables		$M_{\gamma\gamma}$ (GeV)	$M_{j_1 j_2 j_3}$ (GeV)	H_T (GeV)	$\Delta\phi_{Wh}$	$M_T^{W\gamma_1}$ (GeV)
Selection cuts for SR2-A		122–128	>280	>170	>1.4	>170
Signal and background yields	Signal (BP2-A)	115	33	31	27	22
	$t\bar{t}h + \text{jets}$	23	9.0	8.6	5.7	4.8
	$Wh + \text{jets}$	19	5.5	4.7	2.9	2.4
	$Zh + \text{jets}$	4.5	1.1	1.0	0.6	0.4
	$W + \text{jets}$	3.7	0.8	0.6	0.4	0.1
	$Z + \text{jets}$	1.2	0.3	0.1	0.1	0.03
Total background yield: 7.6			Total signal yield: 22		Signal significance: 8.0	
		SR2-B				
Selection cuts for SR2-B		122–128	>300	>120	>1.6	>220
Signal and background yields	Signal (BP2-B)	45	28	28	21	19
	$t\bar{t}h + \text{jets}$	23	8.2	8.1	5.0	3.4
	$Wh + \text{jets}$	19	4.9	4.8	2.7	1.8
	$Zh + \text{jets}$	6.6	1.1	1.0	0.6	0.3
	$W + \text{jets}$	3.7	0.6	0.5	0.3	0
	$Z + \text{jets}$	1.2	0.19	0.19	0.17	0
Total background yield: 5.5			Total signal yield: 20		Signal significance: 8.5	
		SR2-C				
Selection cuts for SR2-C		122–128	>330	>100	>1.5	>220
Signal and background yields	Signal (BP2-C)	10	7.8	7.8	5.5	5.3
	$t\bar{t}h + \text{jets}$	23	7.0	7.0	4.4	2.7
	$Wh + \text{jets}$	19	4.2	4.1	2.5	1.5
	$Zh + \text{jets}$	4.5	0.84	0.84	0.50	0.22
	$W + \text{jets}$	3.7	0.46	0.46	0.18	0
	$Z + \text{jets}$	1.2	0.08	0.08	0.08	0
Total background yield: 4.5			Total signal yield: 5.3		Signal significance: 2.5	

The $M_{j_1 j_2 j_3}$ distribution for the most dominant $t\bar{t}h$ and Wh background peaks roughly at 200 and 75 GeV, respectively, while the $M_{j_1 j_2 j_3}$ peak for the signals heavily depend upon the mass difference between the NLSPs and the χ_1^0 and $m_{\chi_1^0}$. For BP2-A, where both ΔM and $M_{\chi_1^0}$ are relatively smaller (150 and 100 GeV, respectively), the $M_{j_1 j_2 j_3}$ peak mostly overlaps with the $t\bar{t}h$ background. As ΔM and/or $M_{\chi_1^0}$ are increased, as in the case of BP2-B and BP2-C, the peak of the $M_{j_1 j_2 j_3}$ distribution shifts towards higher values and becomes relatively flatter. The H_T variable also displays a similar behavior. The variations in H_T upon changing ΔM or $M_{\chi_1^0}$ are more pronounced as can be seen from Fig. 4(b). The variable, $M_T^{W\gamma_i}$ ($i = 1, 2$), is another important discriminator between the backgrounds and the signal benchmarks with a relatively larger ΔM. In the signal, the mass

difference between the NLPs and χ_1^0 determines the boost carried by the W boson and the Higgs boson. Consequently, the transverse mass of the W system and the photons (produced from h) increases with an increase in ΔM. For the $t\bar{t}h$ and Wh background, $M_T^{W\gamma_1}$ peaks at ~165 and ~150 GeV, respectively. The normalized distribution of BP2-A also peaks roughly at 165 GeV, while BP2-B and BP2-C peak at ~250 and 300 GeV, respectively. The distributions for the latter two also become flatter compared to the distributions for BP2-A and the backgrounds. We also use $\Delta\phi_{Wh}$ while performing the cut-based analysis. We impose a lower limit on $\Delta\phi_{Wh}$ for the three signal benchmarks, details of which can be found in Table II.

The list of selection cuts for these three signal regions along with the cut flow for the three benchmark points have also been tabulated in Table II. The total background yield
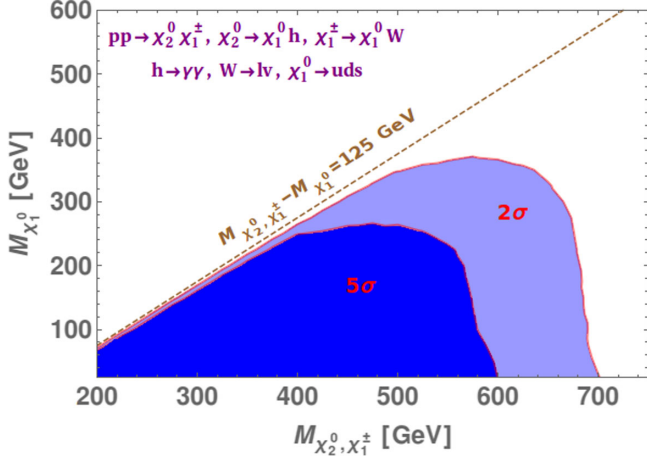
FIG. 5. The projected exclusion (light blue) and discovery (dark blue) regions in the mass plane of $M_{\chi_1^0}$ vs $M_{\chi_2^0,\chi_1^\pm}$ in the Wh simplified model with mass degenerate winolike $\chi_1^\pm, \chi_2^0$ and binolike χ_1^0, and with one RPV term ($\lambda''_{112} u^c d^c s^c$). The brown line denotes the line $M_{\chi_2^0,\chi_1^\pm} - M_{\chi_1^0} = 125$ GeV.

corresponding to the three signal regions, the corresponding signal yields for BP2-A, BP2-B and BP2-C and the signal significances obtained from the cut-based analysis have also been tabulated in Table II. In the current case, SR2-A, SR2-B, SR2-C yield a signal significance of 8.0,8.5,2.5 for BP2-A, BP2-B and BP2-C respectively. It is also worthwhile to note the excellent S/B values for the optimized signal regions. Here, SR2-A, SR2-B and SR2-C result in an exceptional S/B value of 2.89 (for BP2-A), 3.64 (for BP2-B) and 1.18 (for BP2-C), respectively.

The projected 2σ exclusion (light blue) and discovery regions (dark blue) derived from direct wino searches in the Wh mediated $1l + 2\gamma + \text{jets} + \not{E}_T$ final state at the HL-LHC have been shown in the $M_{\chi_1^0} - M_{\chi_2^0,\chi_1^\pm}$ plane, in Fig. 5. The brown dashed line corresponds to the on-shellness condition of h: $M_{\chi_2^0,\chi_1^\pm} - M_{\chi_1^0} = 125$ GeV. It can be observed from Fig. 5 that in the presence of $\lambda''_{112} u^c d^c s^c$-type of RPV operator, direct wino searches at the HL-LHC are projected to exclude winos up to ~ 700 GeV at 2σ and the projected wino discovery reach is up to ~ 600 GeV for a massless χ_1^0.
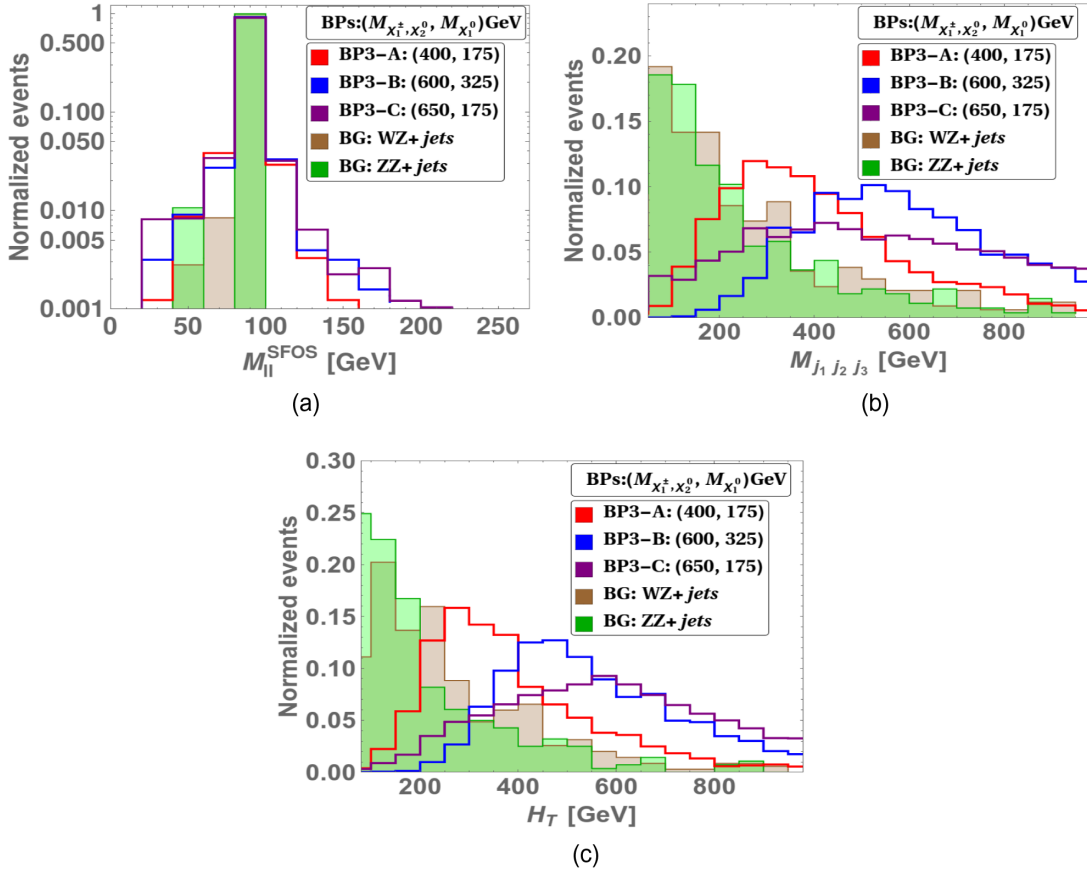

(a)

(b)

(c)

FIG. 6. Normalized distributions of M_{ll}^{SFOS} (a), $M_{j_1 j_2 j_3}$ (b) and H_T (c), for the signal benchmark points, BP3-A (red solid line), BP3-B (blue solid line) and BP3-C (purple solid line), corresponding to the cascade decay process, $pp \to \chi_1^\pm \chi_2^0 \to (\chi_1^\pm \to (W^\pm \to l\nu)(\chi_1^0 \to uds)) (\chi_2^0 \to (Z \to ll) (\chi_1^0 \to uds)) \to 3l + \text{jets} + \not{E}_T$, are shown. The brown and green colored distributions represent the most important background processes: $WZ + \text{jets}$ and $ZZ + \text{jets}$, respectively.

C. Searches in the WZ mediated $3l + \text{jets}(N_j \geq 2) + \not{E}_\text{T}$ channel

A study by the ATLAS Collaboration, which probed the future reach of directly produced winos in the WZ mediated $3l + \not{E}_\text{T}$ final state at the HL-LHC [153], shows a projected exclusion reach up to $M_{\chi_1^\pm \chi_2^0} \sim 1150$ GeV for a binolike $M_{\chi_1^0} \sim 100$ GeV at 95% C.L. The future reach of direct wino searches at HL-LHC in the Wh mediated $3l + \not{E}_\text{T}$ channel has also been studied by ATLAS in [165]. The projected reach excludes winos up to ~650 GeV for $M_{\chi_1^0} \sim 0$ GeV at 95% C.L. One of the main reasons behind the weaker reach of Wh mediated $3l + \not{E}_\text{T}$ channel compared to the WZ mediated process is the longer cascade decay chain in the former case. This results in a smaller event yield even if one assumes a similar signal region efficiency. In the current subsection, we focus only on the analogous

WZ mediated final state reinterpreted in λ''_{112}-type RPV simplified scenario.

In the presence of a λ''_{112}-type RPV coupling, the χ_1^0 would decay into $\chi_1^0 \rightarrow uds$ resulting in WZ mediated $3l + \text{jets} + \not{E}_\text{T}$ final state and the projected exclusions are expected to alter. In the present subsection, we explore this facet and study the projected future reach of WZ mediated $3l + \text{jets} + \not{E}_\text{T}$ final state at the HL-LHC within the framework of a simplified λ''_{112}-type RPV scenario. The Feynman diagram of the signal process under consideration is illustrated in Fig. 1(c). The decay chain proceeds as follows: $pp \rightarrow \chi_1^\pm \chi_2^0 \rightarrow (\chi_1^\pm \rightarrow W\chi_1^0)\ (\chi_2^0 \rightarrow Z\chi_1^0) \rightarrow (W \rightarrow l\nu)\ (\chi_1^0 \rightarrow uds)\ (Z \rightarrow ll)\ (\chi_1^0 \rightarrow uds)$. The SM value for $\text{Br}(Z \rightarrow ll)$ (~6.72% [161]) has been assumed here.

An event is required to have exactly three isolated leptons with $p_T > 30$ GeV and at least two light jets with $p_T > 20$ GeV in the final state. Among the three final

TABLE III. The selection cuts on M_{ll}^SFOS, $\not{E}_\text{T}$, $M_{j_1 j_2 j_3}$ and H_T are listed for the three optimized signal regions: SR3-A, SR3-B and SR3-C, optimized to maximize the signal significance in the WZ mediated $3l + \text{jets} + \not{E}_\text{T}$ final state. The cut flow table showing the signal and background yields upon the successive application of selection cuts is also presented. The maximal value of signal significance obtained from the cut-based optimization procedure is also shown.

SR3-A				
Selection cuts for SR3-A	M_{ll}^SFOS	$M_{j_1 j_2 j_3} > 140$ GeV	$H_T > 220$ GeV	$\cdots$
Signal (BP3-A)	Cut flow of BP3-A: $M_{\chi_2^0,\chi_2^\pm} = 400$ GeV, $M_{\chi_1^0} = 175$ GeV			
	839	808	723	$\cdots$
	Cut flow of backgrounds			
S and B values				
$WZ + \text{jets}$	3.64×10^4	2.47×10^4	1.57×10^4	$\cdots$
$ZZ + \text{jets}$	4146	2408	1219	$\cdots$
$VVV + \text{jets}\ (V = W, Z)$	3069	2130	1568	$\cdots$
Total background yield: 1.85×10^4		Total signal yield: 723		Signal significance: 5.3

SR3-B				
Selection cuts for SR3-B	M_{ll}^SFOS	$M_{j_1 j_2 j_3} > 110$ GeV	$H_T > 280$ GeV	$\cdots$
Signal (BP3-B)	Cut flow of BP3-B: $M_{\chi_2^0,\chi_2^\pm} = 600$ GeV, $M_{\chi_1^0} = 325$ GeV			
	151	151	148	$\cdots$
	Cut flow of backgrounds			
S and B values				
$WZ + \text{jets}$	3.64×10^4	2.74×10^4	1.20×10^4	$\cdots$
$ZZ + \text{jets}$	4146	2853	981	$\cdots$
$VVV + \text{jets}\ (V = W, Z)$	3069	2359	1320	$\cdots$
Total background yield: 1.43×10^4		Total signal yield: 148		Signal significance: 1.2

SR3-C				
Selection cuts for SR3-C	M_{ll}^SFOS	$\not{E}_\text{T} > 150$ GeV	$M_{j_1 j_2 j_3} > 160$ GeV	$H_T > 160$ GeV
Signal (BP3-C)	Cut flow of BP3-C: $M_{\chi_2^0,\chi_2^\pm} = 650$ GeV, $M_{\chi_1^0} = 75$ GeV			
	235	122	115	114
	Cut flow of backgrounds			
S and B values				
$WZ + \text{jets}$	3.6×10^4	3708	2575	2575
$ZZ + \text{jets}$	4146	45	30	15
$VVV + \text{jets}\ (V = W, Z)$	3069	542	384	359
Total background yield: 2950		Total signal yield: 114		Signal significance: 2.1

state leptons, two are required to form a same flavor opposite charge (SFOS) lepton pair with invariant mass in the range of $|M_Z \pm 25 \text{ GeV}|$. In presence of two different SFOS lepton pairs with invariant mass within $|M_Z \pm 25 \text{ GeV}|$, the SFOS pair with invariant mass closest to the Z boson mass is considered to be the correct SFOS pair and their invariant mass is represented as M_{ll}^{SFOS}. The lepton isolation criteria discussed in Sec. II A is applied here as well.

The important sources of background are $WZ + \text{jets}$, $ZZ + \text{jets}$ and $VVV + \text{jets}$ ($V = W, Z$). Potential contribution to background can also arise from $Wh + \text{jets}$ and $Zh + \text{jets}$ processes, however, their contribution is much lesser when compared to the diboson and triboson backgrounds. Consequently, we ignore the contribution from both, $Wh + \text{jets}$ and $Zh + \text{jets}$.

The signal events have been generated for various combinations of $M_{\chi_2^0}(= M_{\chi_1^\pm})$ and $M_{\chi_1^0}$. $M_{\chi_2^0\chi_1^\pm}$ has been varied in between 200 and 1000 GeV with a step size of 25 GeV while $M_{\chi_1^0}$ has been varied from 25 GeV to $M_{\chi_2^0\chi_1^\pm} - M_Z$ with a step size of 10 GeV. Three representative signal benchmark points with small ΔM (BP3-A: $M_{\chi_2^0} = M_{\chi_1^\pm} = 400$ GeV, $M_{\chi_1^0} = 175$ GeV), intermediate ΔM (BP3-B: $M_{\chi_2^0} = M_{\chi_1^\pm} = 600$ GeV, $M_{\chi_1^0} = 325$ GeV) and large ΔM (BP3-C: $M_{\chi_2^0} = M_{\chi_1^\pm} = 650$ GeV, $M_{\chi_1^0} = 175$ GeV) are chosen. Three optimized signal regions are chosen: SR3-A, SR3-B and SR3-C, with optimized selection cuts which maximize the signal significances of BP3-A, BP3-B and BP3-C, respectively. The Appendix lists the cross section of the background and signal benchmark points.

The kinematic variables used to perform the cut-based analysis are invariant mass of the SFOS pair of leptons (M_{ll}^{SFOS}), invariant mass of the three leading p_T ordered jets ($M_{j_1j_2j_3}$), the scalar sum of the transverse momenta of the three leading p_T ordered jets (H_T) and the missing transverse energy ($\not{E}_T$).

$M_{j_1j_2j_3}$ and H_T are observed to be among the most efficient variables in discriminating the signal from the backgrounds. Similar to the observation in Sec. II B, we observe that the peak of $M_{j_1j_2j_3}$ and H_T shifts towards higher values and becomes flatter with increasing ΔM and $M_{\chi_1^0}$. $M_{j_1j_2j_3}$ and H_T peak at $\lesssim 100$ GeV for both the $WZ + \text{jets}$ and the $ZZ + \text{jets}$ background, while all the signal benchmarks peak at values above ~ 250 GeV. The normalized distributions of M_{ll}^{SFOS}, $M_{j_1j_2j_3}$ and H_T for the signal benchmark points, BP3-A (red solid line), BP3-B (blue solid line) and BP3-C (purple solid line), and the most important background processes, $WZ + \text{jets}$ (brown colored region) and $ZZ + \text{jets}$ (green colored region), have been illustrated in Figs 6(a), 6(b) and 6(c), respectively. The selection cuts for the respective signal regions are shown in Table III. The signal and background yields obtained upon the successive application of the selection cuts have also

been listed in Table III along with the respective values of signal significance.

The future reach of direct wino searches in the WZ mediated $3l + \text{jets} + \not{E}_T$ final state at HL-LHC is studied. In this context, we evaluate the projected exclusion ($> 2\sigma$) and projected discovery ($> 5\sigma$) contours assuming zero systematic uncertainty in the $M_{\chi_2^0\chi_1^\pm} - M_{\chi_1^0}$ plane (shown in Fig. 7). The light blue colored region and the dark blue colored regions in Fig. 7 represent the projected exclusion and discovery reach, respectively. The brown dashed line represents the mass correlation: $M_{\chi_1^\pm\chi_2^0} - M_{\chi_1^0} = M_Z$. The projected exclusion region has a reach up to $M_{\chi_2^0\chi_1^\pm} \sim 650$ GeV (winolike) for a binolike $M_{\chi_1^0} \sim 100$ GeV, while the projected discovery region has a potential reach up to $M_{\chi_2^0\chi_1^\pm} \sim 480$ GeV (winolike) for a binolike $M_{\chi_1^0} \sim 100$ GeV. It is to be noted that within the simplified RPC scenario, the projected exclusion contour (at 95% C.L.) of direct wino searches in the WZ mediated $3l + \not{E}_T$ channel at the HL-LHC reaches up to ~ 1150 GeV for a χ_1^0 with mass up to ~ 100 GeV, as evaluated by ATLAS in [153] (shown as green dashed line in Fig. 7). Thus, within the $\lambda_{112}''u^c d^c s^c$-type RPV simplified scenario, the projected reach of HL-LHC in direct wino searches in the $3l + \text{jets} + \not{E}_T$ channel is rendered considerably weaker
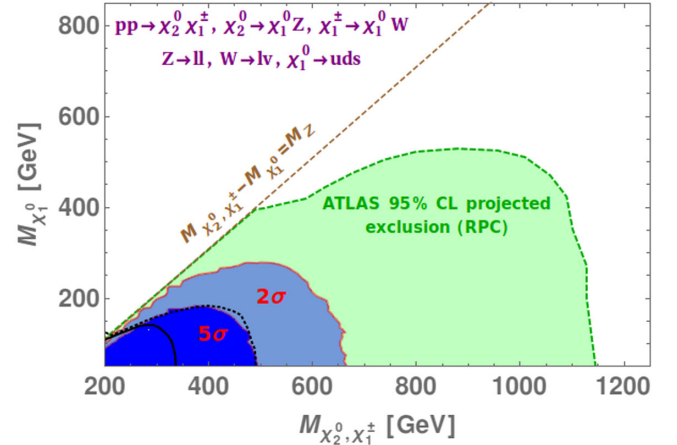

FIG. 7. The projected discovery reach (dark blue) and the projected exclusion reach (light blue) from direct wino searches in the $pp \rightarrow \chi_1^\pm\chi_2^0 \rightarrow 3l + \text{jets} + \not{E}_T$ final state at the HL-LHC ($\sqrt{s} = 14$ TeV, $\mathcal{L} \sim 3$ ab^{-1}) is shown in the $M_{\chi_2^0\chi_1^\pm} - M_{\chi_1^0}$ plane. The solid black and the dashed black line represents the observed limits (at 95% C.L.) derived by ATLAS ($\sqrt{s} = 13$ TeV, $\mathcal{L} \sim 139$ fb^{-1}) [61] and CMS ($\sqrt{s} = 13$ TeV, $\mathcal{L} \sim 36$ fb^{-1}) [153], respectively, from direct wino searches in the WZ mediated $3l + \not{E}_T$ channel within a simplified RPC framework. The light green colored region represents the 95% C.L. projected exclusion region derived by ATLAS [153] from direct wino searches in the $3l + \not{E}_T$ final state at the HL-LHC within a simplified RPC framework. The brown dashed line represents the mass correlation: $M_{\chi_1^\pm\chi_2^0} - M_{\chi_1^0} = M_Z$.

compared to the projected reach of the analogous search in the RPC scenario.

D. Searches in the *WZ* mediated $3l + 2b + \text{jets}(N_j \geq 2) + \not{E}_T$ channel

In the present subsection, we evaluate the HL-LHC prospects of direct wino searches in the *WZ* mediated $3l + 2b + \text{jets} + \not{E}_T$ final state, produced from the cascade decay of directly produced winolike mass degenerate $\chi_2^0 \chi_1^\pm$ pair. Owing to the presence of $\lambda''_{113} u^c d^c b^c$ RPV operator, χ_1^0 decays as $\chi_1^0 \rightarrow udb$. Unlike the previous section, the relevant decay chain proceeds as follows: $pp \rightarrow \chi_1^\pm \chi_2^0 \rightarrow (W\chi_1^0) \, (Z\chi_1^0) \rightarrow (l\nu udb) \, (lludb)$, resulting in *WZ* mediated $3l + 2b + \text{jets} + \not{E}_T$ final state. Although the channel containing $3l$ in the final state is substantially analyzed, $3l + 2b + \text{jets} + \not{E}_T$ final state is not commonly studied in RPC scenario.

The event selection criteria requires the presence of three isolated leptons in the final state along with two *b* jets and at least two light jets. The final state leptons, *b* jets and light jets, are required to have $p_T > 30$ GeV and the pseudorapidity must lie within a range of $|\eta| \leq 2.5$. Here as well,

we demand the presence of at least one SFOS pair out of the final state leptons with invariant mass M_{ll}^{SFOS} in the range of $M_Z \pm 25$ GeV. In the presence of two such SFOS pairs, the one with invariant mass closest to the *Z* boson mass is chosen to be the correct one. The background to the $3l + 2b + \text{jets} + \not{E}_T$ final state is constituted by $t\bar{t}Z$, $VVV + \text{jets}$, $WZ + \text{jets}$ and $ZZ + \text{jets}$ processes.

Three representative benchmark points, BP4-A ($M_{\chi_2^0 \chi_1^\pm} = 250$ GeV, $M_{\chi_1^0} = 135$ GeV), BP4-B ($M_{\chi_2^0 \chi_1^\pm} = 600$ GeV, $M_{\chi_1^0} = 205$ GeV) and BP4-C ($M_{\chi_2^0 \chi_1^\pm} = 700$ GeV, $M_{\chi_1^0} = 85$ GeV), are chosen according to small, medium and large mass splittings between $\chi_2^0(\chi_1^\pm)$ and χ_1^0. Cut-based analysis is performed by optimizing the selection cuts on M_{ll}^{SFOS}, $\not{E}_T$ and H_T to maximize the signal significance. The normalized distribution of M_{ll}^{SFOS}, $\not{E}_T$ and H_T, both for signal and dominant backgrounds has been illustrated in Figs. 8(a), 8(b) and 8(c), respectively. The red, blue and purple solid lines represent the normalized distributions of BP4-A, BP4-B and BP4-C respectively, while the most dominant backgrounds, $t\bar{t}Z$ and $VVV + \text{jets}$, have been represented by green and brown colored regions respectively. Since BP4-A features lower mass difference between
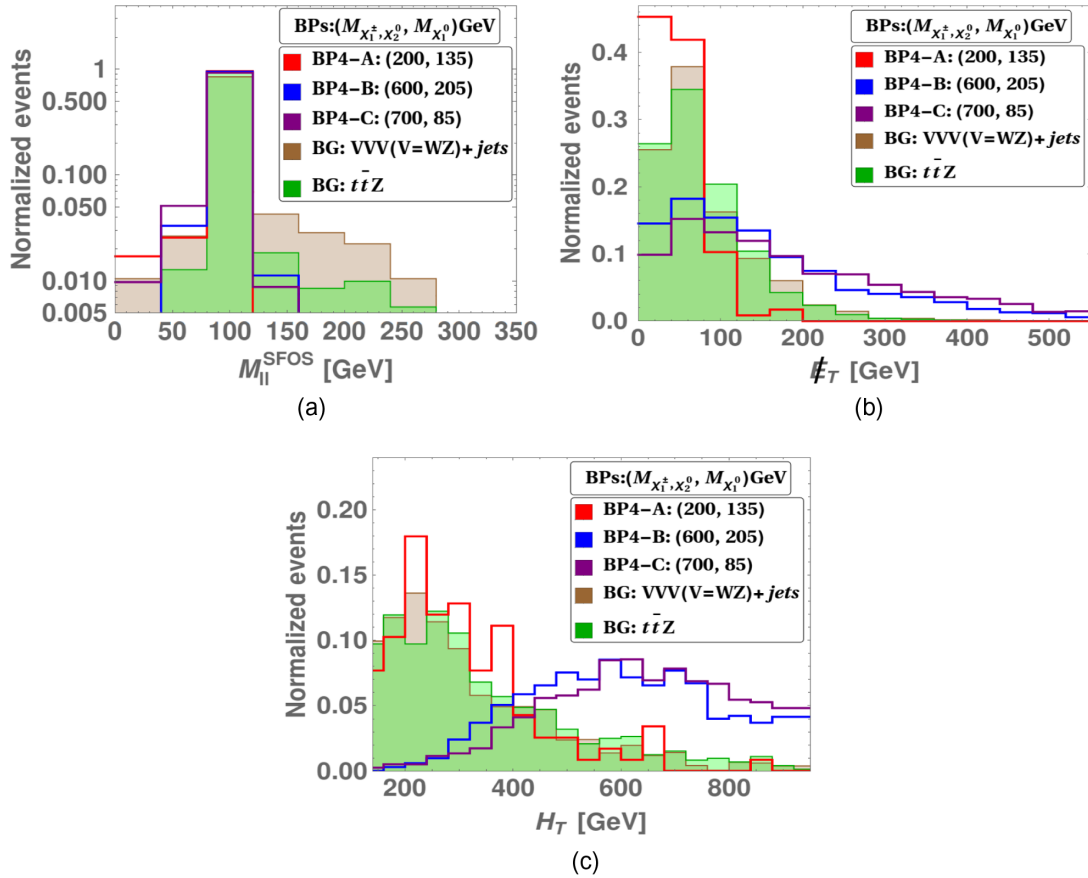

FIG. 8. Normalized distributions of M_{ll}^{SFOS} (a), $\not{E}_T$ (b) and H_T (c) corresponding to the signal benchmark points, BP4-A (red solid line), BP4-B (blue solid line) and BP4-C (purple solid line), in the $3l + 2b + \text{jets} + \not{E}_T$ final state are shown. The respective normalized distributions for the most significant background processes, $t\bar{t}Z$ and $VVV + \text{jets}$, are also displayed as brown and green colored regions, respectively.

TABLE IV. Selection cuts on M_{ll}^{SFOS}, $\not{E}_T$ and H_T are shown along with the cut flow table for the signal and background processes relevant to direct wino searches (in presence of $\lambda''_{113} u^c d^c b^c$-type RPV operator) in the WZ mediated $3l + 2b + \mathrm{jets} + \not{E}_T$ final state. The signal significance values of BP4-A, BP4-B and BP4-C obtained upon the application of selection cuts corresponding to the signal regions, SR4-A, SR4-B and SR4-C, respectively, are also listed.

SR4-A			
Selection cuts for SR4-A	M_{ll}^{SFOS}	$H_T > 250$ GeV	$\cdots$
Signal (BP4-A)	Cut flow of BP4-A: $M_{\chi_2^0,\chi_2^\pm} = 250$ GeV, $M_{\chi_1^0} = 135$ GeV		
	186	128	$\cdots$
	Cut flow of backgrounds		
S and B values $t\bar{t}Z$	1303	1093	$\cdots$
$VVV + \mathrm{jets}$	1571	1353	$\cdots$
$WZ + \mathrm{jets}$	10.4	8.2	$\cdots$
$ZZ + \mathrm{jets}$	9.1	5.3	$\cdots$
Total background yield: 2459.5	Total signal yield: 128	Signal significance: 2.6	

SR4-B			
Selection cuts for SR4-B	M_{ll}^{SFOS}	$\not{E}_T > 160$ GeV	$\cdots$
Signal (BP4-B)	Cut flow of BP4-B: $M_{\chi_2^0,\chi_2^\pm} = 600$ GeV, $M_{\chi_1^0} = 205$ GeV		
	88	34	$\cdots$
	Cut flow of backgrounds		
S and B values $t\bar{t}Z$	1303	98	$\cdots$
$VVV + \mathrm{jets}$	1571	149	$\cdots$
$WZ + \mathrm{jets}$	10.4	3.0	$\cdots$
$ZZ + \mathrm{jets}$	9.1	0.0	$\cdots$
Total background yield: 250	Total signal yield: 34	Signal significance: 2.1	

SR4-C			
Selection cuts for SR4-C	M_{ll}^{SFOS}	$\not{E}_T > 160$ GeV	$H_T > 240$ GeV
Signal (BP4-C)	Cut flow of BP4-C: $M_{\chi_2^0,\chi_2^\pm} = 700$ GeV, $M_{\chi_1^0} = 85$ GeV		
	29	14.5	14.4
	Cut flow of backgrounds		
S and B values $t\bar{t}Z$	1303	98	91
$VVV + \mathrm{jets}$	1571	149	134
$WZ + \mathrm{jets}$	10.4	3.0	2.6
$ZZ + \mathrm{jets}$	9.1	0.0	0.0
Total background yield: 227.6	Total signal yield: 14.3	Signal significance: 0.9	

$\chi_2^0(\chi_1^\pm)$ and χ_1^0 than BP4-B and BP4-C, the light jets emanating from the decay of less boosted χ_1^0 in BP4-A carry relatively smaller p_T as compared to the jets produced from the decay χ_1^0 in the other two benchmark points. This in turn shifts the peak of the H_T distribution towards higher values for BP4-B and BP4-C.

The signal and background cross sections can be seen in the Appendix. The signal significances are optimized for three signal regions: SR4-A, SR4-B and SR4-C. The list of selection cuts on M_{ll}^{SFOS}, $\not{E}_T$ and H_T corresponding to the three signal regions have been itemized in Table IV. The cut flow exhibiting the signal and background yields is also presented in Table IV along with signal significance.

We derive the projected exclusion and discovery contour in the context of HL-LHC, which has been illustrated in light blue and dark blue colors, respectively, in Fig. 9. The brown dashed line corresponds to the mass correlation: $M_{\chi_1^\pm,\chi_2^0} - M_{\chi_1^0} = M_Z$. The projected exclusion region reaches up to $M_{\chi_1^\pm,\chi_2^0} \sim 600$ GeV for winolike $\chi_1^\pm,\chi_2^0$ and binolike χ_1^0 with mass in the range $\sim[150\text{–}250]$ GeV.

Thus, we observe that a variety of interesting multiparticle final states can be produced from the cascade decay of direct wino production on account of the introduction of R-parity violating operators, many of which display a strong potential to be excluded and even discovered at the HL-LHC. In the present work, we explored the future prospects of two different types of RPV operator,
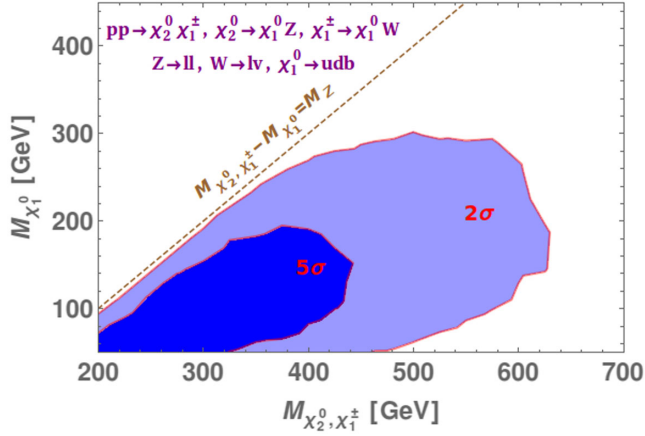
FIG. 9. The projected discovery (dark blue colored) and exclusion (light blue colored) regions for direct wino searches in the $3l + 2b + \text{jets} + \not{E}_T$ channel at the HL-LHC. The final state is an implication of $\lambda''_{113} u^c d^c b^c$-type RPV operator which implies $\chi_1^0 \rightarrow udb$. The brown line corresponds to $M_{\chi_2^0, \chi_1^\pm} - M_{\chi_1^0} = M_Z$.

$\lambda''_{112} u^c d^c s^c$ (in Wh mediated $1l + 2b + \text{jets} + \not{E}_T$ channel, Wh mediated $1l + 2\gamma + \text{jets} + \not{E}_T$ channel, WZ mediated $3l + \text{jets} + \not{E}_T$ channel) and $\lambda''_{113} u^c d^c b^c$ (in WZ mediated $3l + 2b + \text{jets} + \not{E}_T$ channel) by performing a detailed cut-based analysis involving all relevant background processes. We intend to evaluate the implications from various other types of RPV operators on a multitude of search channels in an ongoing work. A more sophisticated analysis of the underlying final state jets and better understanding of the multiparticle backgrounds might help in further improving the future discovery prospects in these channels. Before concluding this work, we briefly discuss the implications from pure-higgsino searches and also analyze the projected sensitivity for a few realistic MSSM benchmark points where the neutralinos and charginos are gaugino-higgsino admixtures.

III. BENCHMARK SCENARIOS

We begin our discussion in this section by considering two benchmark points with higgsinolike $\chi_2^0, \chi_3^0, \chi_1^\pm$ and binolike χ_1^0; BP-$\alpha_{\tilde{H}}$ ($M_{\chi_3^0 \chi_2^0 \chi_1^\pm} = 450$ GeV, $M_{\chi_1^0} = 150$ GeV) and BP-$\beta_{\tilde{H}}$ ($M_{\chi_3^0 \chi_2^0 \chi_1^\pm} = 500$ GeV, $M_{\chi_1^0} = 200$ GeV), and contrast their projected detectability at the HL-LHC with their pure wino counterparts: BP-$\alpha_{\tilde{W}}$ ($M_{\chi_2^0 \chi_1^\pm} = 450$ GeV, $M_{\chi_1^0} = 150$ GeV) and BP-$\beta_{\tilde{W}}$ ($M_{\chi_2^0 \chi_1^\pm} = 500$ GeV, $M_{\chi_1^0} = 200$ GeV), for the four signal channels considered in this work. BP-$\alpha_{\tilde{W}}$ and BP-$\beta_{\tilde{W}}$ fall within the projected exclusion reach of direct wino searches in the Wh mediated $1l + 2b + \text{jets} + \not{E}_T$ final state (see Fig. 3). However, direct higgsino searches in the same search channel result in a signal significance of ~ 1.56 and ~ 0.83 for their pure-higgsino counterparts BP-$\alpha_{\tilde{H}}$ and BP-$\beta_{\tilde{H}}$, respectively, thereby, putting both these benchmark points outside the projected exclusion region. BP-$\alpha_{\tilde{W}}$ also falls within the projected discovery reach of direct wino searches in the other three search channels (see Figs. 5, 7 and 9). However, direct higgsino searches (for BP-$\alpha_{\tilde{H}}$) result in a signal significance of ~ 2.94, ~ 2.30 and ~ 1.76 in Wh mediated $1l + 2\gamma + \text{jets} + \not{E}_T$, WZ mediated $3l + \text{jets} + \not{E}_T$ and WZ mediated $3l + 2b + \text{jets} + \not{E}_T$ search channels, respectively, and thus, BP-$\alpha_{\tilde{H}}$ falls within (outside) the projected exclusion (discovery) reach of the aforementioned former two channels and even outside the projected exclusion region of the later search channel. BP-$\beta_{\tilde{W}}$ also falls within the projected discovery reach of direct wino searches in the Wh mediated $1l + 2\gamma + \text{jets} + \not{E}_T$ channel, and within the projected exclusion reach in the WZ mediated $3l + \text{jets} + \not{E}_T$ and WZ mediated $3l + 2b + \text{jets} + \not{E}_T$. On the contrary, in direct higgsino searches, the signal significance of BP-$\beta_{\tilde{H}}$ marginally crosses 2σ in the Wh mediated $1l + 2\gamma + \text{jets} + \not{E}_T$ channel, while registering a value of ~ 1.66 and ~ 1.4 in the WZ mediated $3l + \text{jets} + \not{E}_T$ and WZ mediated $3l + 2b + \text{jets} + \not{E}_T$ channels,

TABLE V. The $\chi_1^\pm \chi_2^0$ production cross section and $\text{Br}(\chi_2^0 \rightarrow Z/h\chi_1^0)$ are shown against the different $\tan\beta$ values for BP-$\beta_{\tilde{W}}$. The respective signal significance values in the 4 analysis channels (3 signal regions in each channel) considered in this work are also listed.

| | | | Signal Significance | | | | | | | | | | | |
| | | | Wh mediated $1l+2b+\text{jets}+\not{E}_T$ | | | Wh mediated $1l+2\gamma+\text{jets}+\not{E}_T$ | | | WZ mediated $3l+\text{jets}+\not{E}_T$ | | | WZ mediated $3l+2b+\text{jets}+\not{E}_T$ | | |
$\tan\beta$	$\sigma(\chi_1^\pm \chi_2^0)$ (fb)	$\text{Br}(\chi_2^0 \rightarrow Z\chi_1^0)$ (%)	$\text{Br}(\chi_2^0 \rightarrow h\chi_1^0)$ (%)	SR1-A	SR1-B	SR1-C	SR2-A	SR2-B	SR2-C	SR3-A	SR3-B	SR3-C	SR4-A	SR4-B	SR4-C
5	22.65	1.65	98.34	0.49	0.73	0.92	1.57	1.60	2.15	0.14	0.14	0.13	0.001	0.004	0.004
8	22.80	3.26	96.74	0.49	0.72	0.91	1.56	1.58	2.13	0.27	0.28	0.26	0.003	0.009	0.007
10	22.79	4.25	95.74	0.48	0.71	0.90	1.54	1.57	2.11	0.35	0.37	0.34	0.004	0.01	0.009
15	22.48	6.35	93.64	0.46	0.69	0.87	1.49	1.51	2.03	0.52	0.54	0.50	0.006	0.02	0.01
20	22.47	7.98	92.01	0.45	0.68	0.85	1.46	1.48	2.00	0.66	0.68	0.63	0.008	0.02	0.02
25	22.74	9.25	90.74	0.45	0.68	0.85	1.46	1.48	1.99	0.77	0.80	0.74	0.009	0.02	0.02
30	22.65	10.26	89.73	0.45	0.66	0.84	1.44	1.46	1.96	0.85	0.88	0.82	0.01	0.03	0.02
40	22.65	11.77	88.22	0.44	0.65	0.82	1.41	1.43	1.93	0.98	1.01	0.94	0.01	0.03	0.03

respectively. The direct higgsino searches, thus, imply weaker exclusion reach than the analogous wino counterparts, mainly, due to a smaller production cross section.

In the MSSM, the tree level electroweakino sector is governed by four input parameters: M_1 (bino mass parameter), M_2 (wino mass parameter), μ (higgsino mass parameter) and $\tan\beta$ (ratio of vacuum expectation value of the two Higgs doublets). We first consider the case of BP-$\beta_{\tilde{W}}$ ($M_1 \sim 200$ GeV, $M_2 \sim 500$ GeV, $\mu \sim 2$ TeV) and study the collider implications of varying $\tan\beta$. In this respect, we consider 8 benchmark points with different values of $\tan\beta \sim 5, 8, 10, 15, 20, 25, 30, 40$ (M_1, M_2 and μ are kept fixed at the aforesaid values) and compute their signal significance in the 4 signal channels considered in this work. In these benchmark points, the sleptons and the squarks have been decoupled by fixing their masses at ~ 3 TeV and ~ 1.5 TeV, respectively. In the case of BP-$\beta_{\tilde{W}}$, $\chi_3^0, \chi_4^0, \chi_2^\pm$ have a dominant higgsino composition with a mass of ~ 2 TeV. Being heavier, the direct production cross section of the chargino-neutralino pairs involving any of these higgsinolike inos is negligible compared to the production cross section of the winolike $\chi_1^\pm\chi_2^0$ pair. Consequently, we only consider the direct production of $\chi_1^\pm\chi_2^0$ pair while computing the signal significance and ignore the contributions from the other ino pairs. Here, the

signal yield is computed in each of the 4 signal channels by multiplying the $\chi_1^\pm\chi_2^0$ pair production cross section $[\sigma(\chi_1^\pm\chi_2^0)]$ with the branching rates of the relevant cascade decay modes, the integrated luminosity ($\mathcal{L} = 3000$ fb^{-1}) and the efficiency of the respective signal regions. In the case of Wh mediated signal channels (Wh mediated $1l + 2b + \text{jets} + \not{E}_T$ and Wh mediated $1l + 2\gamma + \text{jets} + \not{E}_T$), the relevant ino branching modes are $\text{Br}(\chi_2^0 \to h\chi_1^0)$ and $\text{Br}(\chi_1^\pm \to W\chi_1^0)$, while the relevant ino decay modes in the later two cases (WZ mediated $3l + \text{jets} + \not{E}_T$ and WZ mediated $3l + 2b + \text{jets} + \not{E}_T$) are $\text{Br}(\chi_2^0 \to Z\chi_1^0)$ and $\text{Br}(\chi_1^\pm \to W\chi_1^0)$. The SM branching rates are considered for the successive decay of Z, h and W bosons. Prospino [166,167] is used to compute $\sigma(pp \to \chi_1^\pm\chi_2^0)$ at NLO while SUSY-HIT [168] is used to compute the ino branching rates. The corresponding ino pair production cross section and the ino branching rates are dependent on $\tan\beta$ and have been shown in Table V against their respective $\tan\beta$ values. We have also listed the respective signal significance values in the 12 signal regions (4 different analysis channels $\times 3$ signal regions in each) in Table V.

The coupling of the Z boson with a pair of neutralinos $[\chi_i^0\chi_j^0$ ($i, j = 1, 2, 3, 4)]$ is crucially controlled by the higgsino composition of $\chi_{i,j}^0$ while the $h\chi_i^0\chi_j^0$ couplings are
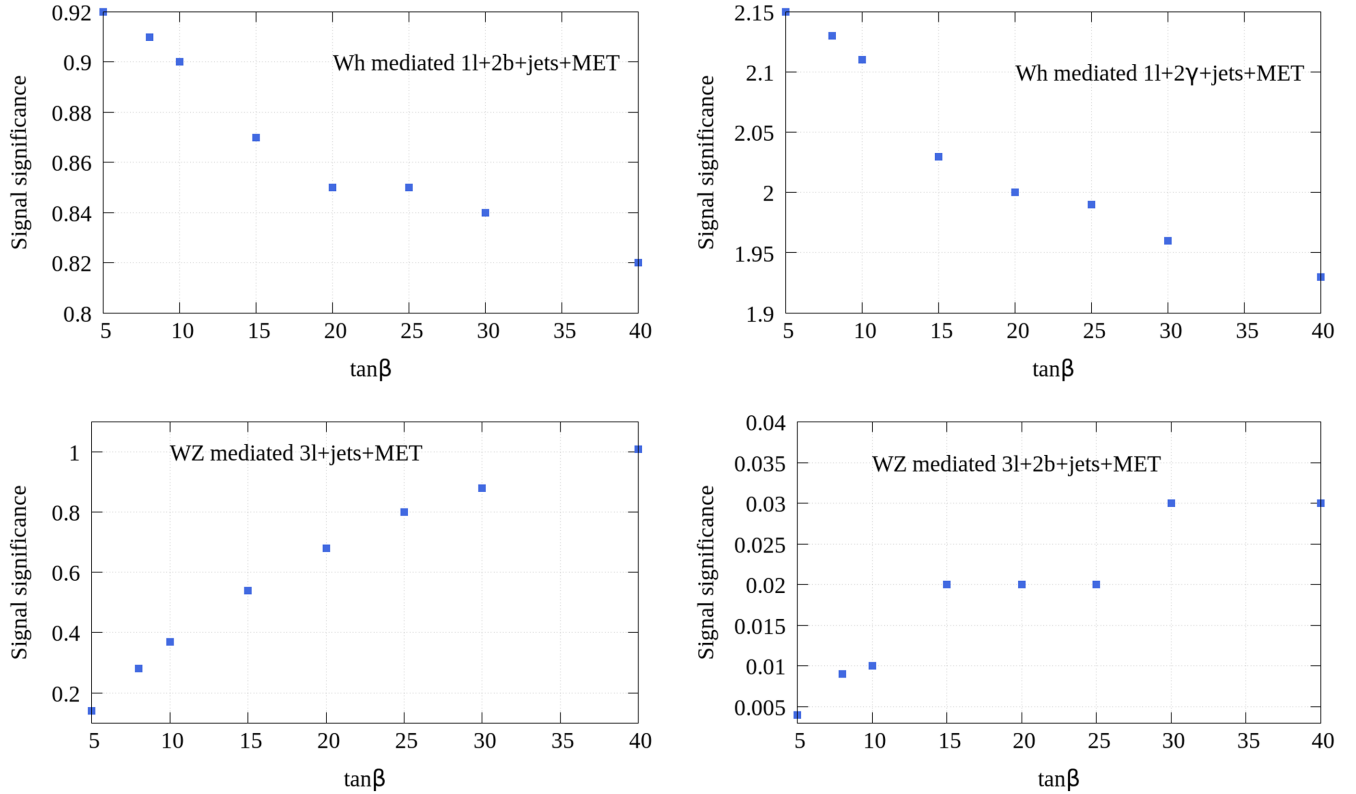

FIG. 10. The largest signal significance value in a particular signal channel and $\tan\beta$ are shown along the y and x axes. The WZ mediated and Wh mediated channels exhibit an opposite behavior with variations in $\tan\beta$. The signal significance values fall and rise with increase in $\tan\beta$ for the Wh mediated and WZ mediated channels, respectively. Here, MET refers to $\not{E}_T$.

proportional to the gaugino-higgsino admixture in $\chi_{i,j}^0$. As stated earlier, the tree level neutralino mixing matrix is governed by M_1, M_2, μ and $\tan\beta$. Thereby, the $Z\chi_i^0\chi_j^0$ and $h\chi_i^0\chi_j^0$ couplings are also controlled by the same input parameters at the tree level. In the present case, χ_2^0 is dominantly wino in nature with a small higgsino component (which varies with $\tan\beta$) in all the 8 benchmark points. This makes $\chi_2^0 \to \chi_1^0 h$ as the most preferable decay mode of χ_2^0 with a branching ratio of $\sim 98.34\%$ for $\tan\beta = 5$. However, $\mathrm{Br}(\chi_2^0 \to \chi_1^0 h)$ decreases up to $\sim 88.22\%$ upon increasing $\tan\beta$ to 40. Correspondingly, $\mathrm{Br}(\chi_2^0 \to \chi_1^0 Z)$ increases from $\sim 1.65\%$ at $\tan\beta = 5$ up to $\sim 11.77\%$ at $\tan\beta = 40$, thus, registering a nearly ~ 7 times improvement. The increase in the branching rate of $\chi_2^0 \to \chi_1^0 Z$ is reflected in the signal significance of WZ mediated analysis channels (shown in Table V and bottom panel of Fig. 10). The signal significance of SR3-A, SR3-B and SR3-C (the optimized signal regions corresponding to WZ mediated $3l + \text{jets} + \not{E}_T$ channel) increases from 0.14,0.14 and 0.13 (at $\tan\beta = 5$) to 0.98, 1.01 and 0.94, respectively, at $\tan\beta = 40$. A similar increase is also evident in the signal significance of SR4-A, SR4-B and SR4-C (signal regions corresponding to the WZ mediated $3l + 2b + \text{jets} + \not{E}_T$ channel) which have a value of 0.001, 0.004 and 0.004, respectively, at $\tan\beta = 5$ while the respective values at $\tan\beta = 40$ are 0.01, 0.03 and 0.03. Equivalently, the signal significance of the Wh mediated signal channels decrease with increasing $\tan\beta$. In Fig. 10, we have illustrated the variation of the signal significance (shown along y axis) of

the 4 analysis channels considered in this work with $\tan\beta$ (shown along x axis) for BP-$\beta_{\tilde{W}}$. For a particular final state, the largest value of signal significance among the respective 3 signal regions has been considered in Fig. 10.

We also analyze additional realistic benchmark scenarios where we vary the higgsino and wino admixtures in the neutralinos and charginos, and study the projected reach of HL-LHC in probing them in the Wh mediated $1l + 2b + \text{jets} + \not{E}_T$, Wh mediated $1l + 2\gamma + \text{jets} + \not{E}_T$, WZ mediated $3l + \text{jets} + \not{E}_T$ and WZ mediated $3l + 2b + \text{jets} + \not{E}_T$ final states. We choose four different benchmark points (BP-$\beta_{\tilde{W}}^{10}$, BP-$\beta_{\tilde{W}}^{30}$, BP-$\beta_{\tilde{W}}^{50}$ and BP-$\beta_{\tilde{W}}^{70}$) in such a way that $M_{\chi_2^0}$ and $M_{\chi_1^\pm}$ are always at roughly ~ 500 GeV while $M_{\chi_1^0}$ is at roughly ~ 200 GeV. We also ensure than χ_1^0 is always binolike by fixing M_1 at 200 GeV. The sleptons, squarks and gluinos are fixed at ~ 3, ~ 1.5 and ~ 4 TeV, respectively, in order to decouple their effects from the processes of our interest. The value of $\tan\beta$ is fixed to 10. M_2 and μ are varied such that the amount of higgsino component in χ_2^0 is $\sim 10\%$ (BP-$\beta_{\tilde{W}}^{10}$), $\sim 30\%$ (BP-$\beta_{\tilde{W}}^{30}$), $\sim 50\%$ (BP-$\beta_{\tilde{W}}^{50}$) and $\sim 70\%$ (BP-$\beta_{\tilde{W}}^{70}$). The values of M_2 and μ for these 4 benchmark points along with their electroweakino mass spectrum are shown in Table VI. We have also listed the higgsino and wino composition in Table VI.

In the previous case of BP-$\beta_{\tilde{W}}$, the amount of higgsino admixture in χ_2^0 was $\lesssim 1\%$ for $\tan\beta = 10$. Also, χ_3^0, χ_4^0 and $\chi_2^\pm$ were much heavier (~ 2 TeV) and therefore, the contributions to the signal yield from $\chi_2^0\chi_1^\pm$, $\chi_3^0\chi_1^\pm$, $\chi_4^0\chi_1^\pm$, $\chi_3^0\chi_2^\pm$ and $\chi_4^0\chi_2^\pm$ production processes could be safely ignored due

TABLE VI. The electroweakino mass spectrum of BP-$\beta_{\tilde{W}}^{10}$, BP-$\beta_{\tilde{W}}^{30}$, BP-$\beta_{\tilde{W}}^{50}$ and BP-$\beta_{\tilde{W}}^{70}$ is shown along with the values of M_2 and μ. The wino and higgsino compositions of the electroweakinos are also listed. The NLO cross section of directly produced chargino-neutralino pairs and the electroweakino branching fractions which are relevant to the 4 signal channels analyzed in this work are shown. Here, $\chi_1^\pm$ always decays into $W\chi_1^0$. The signal significance values in the respective analysis channels are also tabulated.

BP-$\beta_{\tilde{W}}^{10}$ ($M_2 = 515$ GeV, $\mu = 670$ GeV)					
EW inos	χ_1^0	χ_2^0	χ_3^0	χ_4^0	$\chi_1^\pm$ $\chi_2^\pm$

EW inos	χ_1^0	χ_2^0	χ_3^0	χ_4^0	$\chi_1^\pm$	$\chi_2^\pm$
Mass (in GeV)	198.35	496.45	672.90	693.11	496.28	692.73
wino %	10^{-3}	89.36	0.16	10.43	86.67	13.19
higgsino %	0.65	10.51	99.68	88.99	13.19	86.67
Cross-section	$\sigma(\chi_1^\pm\chi_2^0)$ 21.94	$\sigma(\chi_1^\pm\chi_3^0)$ 0.72	$\sigma(\chi_1^\pm\chi_4^0)$ 0.3	$\sigma(\chi_2^\pm\chi_2^0)$ 0.02	$\sigma(\chi_2^\pm\chi_3^0)$ 2.93	$\sigma(\chi_2^\pm\chi_4^0)$ 2.99

Relevant Brs (%)	$\chi_2^0 \to \chi_1^0 Z$ (10.4), $\chi_2^0 \to \chi_1^0 h$ (89.5), $\chi_3^0 \to \chi_1^0 Z$ (15.86), $\chi_3^0 \to \chi_1^0 h$ (2.97), $\chi_4^0 \to \chi_1^0 Z$ (2.74), $\chi_4^0 \to \chi_1^0 h$ (12.55), $\chi_2^0 \to W\chi_1^0$ (14.20)

Signal significance	Wh mediated $1l + 2b + \text{jets} + \not{E}_T$			Wh mediated $1l + 2\gamma + \text{jets} + \not{E}_T$			WZ mediated $3l + \text{jets} + \not{E}_T$			WZ mediated $3l + 2b + \text{jets} + \not{E}_T$		
	SR1-A	SR1-B	SR1-C	SR2-A	SR2-B	SR2-C	SR3-A	SR3-B	SR3-C	SR4-A	SR4-B	SR4-C
	0.44	0.64	0.24	1.39	1.41	1.90	0.09	0.09	0.06	0.03	0.09	0.06

BP-$\beta_{\tilde{W}}^{30}$ ($M_2 = 540$ GeV, $\mu = 590$ GeV)					
EW inos	χ_1^0	χ_2^0	χ_3^0	χ_4^0	$\chi_1^\pm$ $\chi_2^\pm$

EW inos	χ_1^0	χ_2^0	χ_3^0	χ_4^0	$\chi_1^\pm$	$\chi_2^\pm$
Mass (in GeV)	197.92	502.28	593.09	632.89	501.79	632.41
wino %	0.01	69.33	0.18	30.46	65.09	34.90

(Table continued)

TABLE VI. *(Continued)*

	χ_1^0	χ_2^0	χ_3^0	χ_4^0	$\chi_1^\pm$	$\chi_2^\pm$
BP-$\beta_{\tilde{W}}^{30}$ ($M_2 = 540$ GeV, $\mu = 590$ GeV)						
EW inos	χ_1^0	χ_2^0	χ_3^0	χ_4^0	$\chi_1^\pm$	$\chi_2^\pm$
higgsino %	0.92	30.31	99.67	69.06	34.90	65.09
Cross-section	$\sigma(\chi_1^\pm\chi_2^0)$	$\sigma(\chi_1^\pm\chi_3^0)$	$\sigma(\chi_1^\pm\chi_4^0)$	$\sigma(\chi_2^\pm\chi_2^0)$	$\sigma(\chi_2^\pm\chi_3^0)$	$\sigma(\chi_2^\pm\chi_4^0)$
	18.91	2.86	0.13	0.10	3.77	4.78

Relevant Brs (%) $\quad$ $\chi_2^0 \to \chi_1^0 Z$ (11.62), $\chi_2^0 \to \chi_1^0 h$ (88.37), $\chi_3^0 \to \chi_1^0 Z$ (69.17), $\chi_3^0 \to \chi_1^0 h$ (10.60), $\chi_4^0 \to \chi_1^0 Z$ (4.09), $\chi_4^0 \to \chi_1^0 h$ (19.8), $\chi_2^\pm \to W\chi_1^0$ (24.00)

Signal significance $\quad$ Wh mediated $1l+2b+\text{jets}+\not{E}_T$ $\quad$ Wh mediated $1l+2\gamma+\text{jets}+\not{E}_T$ $\quad$ WZ mediated $3l+\text{jets}+\not{E}_T$ $\quad$ WZ mediated $3l+2b+\text{jets}+\not{E}_T$

SR1-A	SR1-B	SR1-C	SR2-A	SR2-B	SR2-C	SR3-A	SR3-B	SR3-C	SR4-A	SR4-B	SR4-C
0.39	0.55	0.69	1.24	1.25	1.68	0.21	0.11	0.09	0.29	0.78	0.39

	χ_1^0	χ_2^0	χ_3^0	χ_4^0	$\chi_1^\pm$	$\chi_2^\pm$
BP-$\beta_{\tilde{W}}^{50}$ ($M_2 = 555$ GeV, $\mu = 550$ GeV)						
EW inos	χ_1^0	χ_2^0	χ_3^0	χ_4^0	$\chi_1^\pm$	$\chi_2^\pm$
Mass (in GeV)	197.62	495.15	553.19	615.41	494.27	615.03
wino %	0.01	48.29	0.19	51.49	43.53	56.44
higgsino %	1.12	51.04	99.66	48.15	56.44	43.53
Cross-section	$\sigma(\chi_1^\pm\chi_2^0)$	$\sigma(\chi_1^\pm\chi_3^0)$	$\sigma(\chi_1^\pm\chi_4^0)$	$\sigma(\chi_2^\pm\chi_2^0)$	$\sigma(\chi_2^\pm\chi_3^0)$	$\sigma(\chi_2^\pm\chi_4^0)$
	18.61	5.90	0.13	0.15	3.26	5.75

Relevant Brs (%) $\quad$ $\chi_2^0 \to \chi_1^0 Z$ (11.91), $\chi_2^0 \to \chi_1^0 h$ (88.08), $\chi_3^0 \to \chi_1^0 Z$ (88.12), $\chi_3^0 \to \chi_1^0 h$ (11.88), $\chi_4^0 \to \chi_1^0 Z$ (3.53), $\chi_4^0 \to \chi_1^0 h$ (16.85), $\chi_2^\pm \to W\chi_1^0$ (21.20)

Signal significance $\quad$ Wh mediated $1l+2b+\text{jets}+\not{E}_T$ $\quad$ Wh mediated $1l+2\gamma+\text{jets}+\not{E}_T$ $\quad$ WZ mediated $3l+\text{jets}+\not{E}_T$ $\quad$ WZ mediated $3l+2b+\text{jets}+\not{E}_T$

SR1-A	SR1-B	SR1-C	SR2-A	SR2-B	SR2-C	SR3-A	SR3-B	SR3-C	SR4-A	SR4-B	SR4-C
0.39	0.54	0.68	1.24	1.26	1.68	0.34	0.13	0.11	0.55	1.43	0.65

BP-$\beta_{\tilde{W}}^{70}$ ($M_2 = 600$ GeV, $\mu = 535$ GeV)

EW inos	χ_1^0	χ_2^0	χ_3^0	χ_4^0	$\chi_1^\pm$	$\chi_2^\pm$
Mass (in GeV)	197.49	502.35	538.15	638.31	501.11	638.11
wino %	0.01	26.54	0.18	73.26	22.60	80.56
higgsino %	1.21	72.54	99.66	26.54	80.56	22.60
Cross-section	$\sigma(\chi_1^\pm\chi_2^0)$	$\sigma(\chi_1^\pm\chi_3^0)$	$\sigma(\chi_1^\pm\chi_4^0)$	$\sigma(\chi_2^\pm\chi_2^0)$	$\sigma(\chi_2^\pm\chi_3^0)$	$\sigma(\chi_2^\pm\chi_4^0)$
	15.31	6.74	0.08	0.09	1.70	4.67

Relevant Brs (%) $\quad$ $\chi_2^0 \to \chi_1^0 Z$ (12.45), $\chi_2^0 \to \chi_1^0 h$ (87.55), $\chi_3^0 \to \chi_1^0 Z$ (88.68), $\chi_3^0 \to \chi_1^0 h$ (11.32), $\chi_4^0 \to \chi_1^0 Z$ (6.03), $\chi_4^0 \to \chi_1^0 h$ (5.44), $\chi_2^\pm \to W\chi_1^0$ (6.78)

Signal significance $\quad$ Wh mediated $1l+2b+\text{jets}+\not{E}_T$ $\quad$ Wh mediated $1l+2\gamma+\text{jets}+\not{E}_T$ $\quad$ WZ mediated $3l+\text{jets}+\not{E}_T$ $\quad$ WZ mediated $3l+2b+\text{jets}+\not{E}_T$

SR1-A	SR1-B	SR1-C	SR2-A	SR2-B	SR2-C	SR3-A	SR3-B	SR3-C	SR4-A	SR4-B	SR4-C
0.32	0.44	0.55	1.01	1.02	1.37	0.34	0.12	0.10	0.58	1.50	0.68

to their small cross sections. However, in the present case, when we attempt to introduce a finite amount of higgsino admixture in χ_2^0 while keeping its mass fixed at ~ 500 GeV, we are forced to reduce the value of μ. Consequently, χ_3^0, χ_4^0 and $\chi_2^\pm$ are no more in the $\sim O(1)$ TeV range. For example, in the case of BP-$\beta_{\tilde{W}}^{10}$ where the χ_2^0 is composed of higgsinos and winos in the proportion of $\sim 10\%$ and $\sim 90\%$, respectively, we are required to choose $\mu \sim 670$ GeV. As a result, χ_3^0, χ_4^0 and $\chi_2^\pm$ also become admixtures of winos and higgsinos and have a mass of ~ 672.90, ~ 693.11 and ~ 692.73 GeV, respectively. Correspondingly, it would be imperative to take into account the contributions from the heavier chargino-neutralino pairs as well. In the present scenario, therefore, contributions to the signal yield can potentially arise from $pp \to \chi_1^\pm\chi_2^0 + \chi_1^\pm\chi_3^0 + \chi_1^\pm\chi_4^0 +$

$\chi_2^\pm\chi_2^0 + \chi_2^\pm\chi_3^0 + \chi_2^\pm\chi_4^0$. The production cross section of these chargino-neutralino pairs for BP-$\beta_{\tilde{W}}^{10}$, BP-$\beta_{\tilde{W}}^{30}$, BP-$\beta_{\tilde{W}}^{50}$ and BP-$\beta_{\tilde{W}}^{70}$ are listed in Table VI. Here, we have used Prospino-2.1 to compute the cross sections at NLO. The branching ratios of $\chi_i^0 \to Z/h\chi_1^0$ ($i = 2, 3, 4$) and $\chi_j^\pm \to W\chi_1^0$ ($j = 1, 2$) are also shown in Table VI where SUSY-HIT has been used to compute them. The signal significance of these 4 benchmark points is computed for (SR1-A, SR1-B, SR1-C), (SR2-A, SR2-B, SR2-C), (SR3-A, SR3-B, SR3-C) and (SR4-A, SR4-B, SR4-C), corresponding to Wh mediated $1l + 2b + \text{jets} + \not{E}_T$, Wh mediated $1l + 2\gamma + \text{jets} + \not{E}_T$, WZ mediated $3l + \text{jets} + \not{E}_T$ and WZ mediated $3 + 2b + \text{jets} + \not{E}_T$ channels, respectively, and have been listed in Table VI. It can be observed from Table VI that the signal significance of the WZ mediated channels improve with an
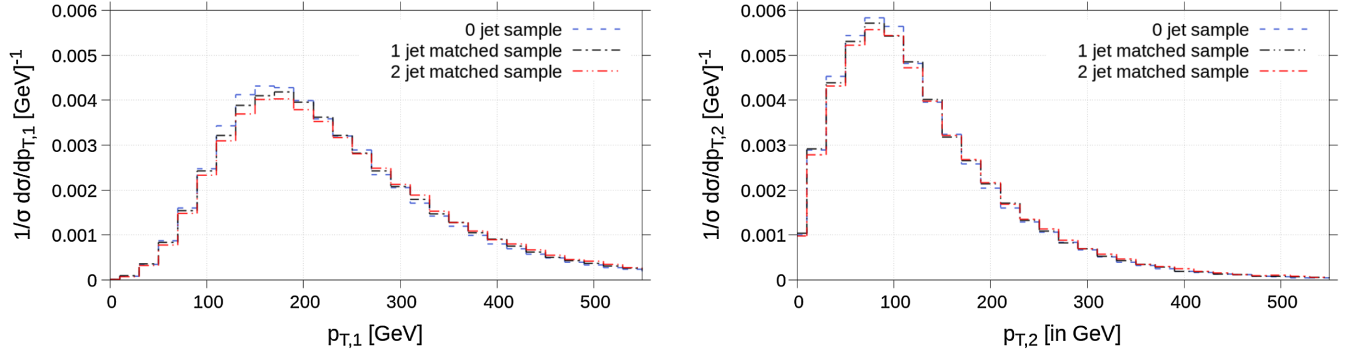
FIG. 11.   Normalized distributions illustrating the p_T of the χ_1^0's produced via $pp \to \chi_1^\pm \chi_2^0 \to (W^\pm \chi_1^0)(Z\chi_1^0)$ at the HL-LHC. $p_{T,1}$ (left panel) and $p_{T,2}$ (right panel) represents the transverse momentum of the χ_1^0 with the highest and the second highest p_T. The distributions correspond to 2 jet (red dot-dot-dashed line), 1 jet (black dot-dashed line) and 0 jet matched (blue dashed line) samples.

increase in the amount of higgsino content in χ_2^0. For example, the signal significance of SR3-A and SR4-A increases from ~0.09 and ~0.03 for BP-$\beta_{\tilde{W}}^{10}$ to ~0.34 and ~0.58 for BP-$\beta_{\tilde{W}}^{70}$. This increase is mainly an outcome of the combined effect of an increased $\chi_2^0/\chi_3^0 \to Z\chi_1^0$ branching rate, an increased $\sigma(\chi_3^0\tilde{\chi}_1^\pm)$ and a lowered $\sigma(\chi_2^0\tilde{\chi}_1^\pm)$. Upon combining the highest signal significance values in each of the analysis channels in quadrature, we obtain a combined signal significance of 2.01, 1.98, 2.33 and 2.12 for BP-$\beta_{\tilde{W}}^{10}$, BP-$\beta_{\tilde{W}}^{30}$, BP-$\beta_{\tilde{W}}^{50}$ and BP-$\beta_{\tilde{W}}^{70}$, respectively. Before concluding this section, we would like to note that additional contribution to the signal yield may also arise by considering the cascade decay modes of the heavier charginos and neutralinos. For example, in a generic case, the χ_3^0 can decay into a $Z/h\chi_2^0$ pair and this χ_2^0 can further decay into a $Z/h\chi_1^0$ pair, resulting in an additional Z/h bosons in the final state. A multifarious number of such possibilities is potentially feasible, and are outside the scope of this present work. We intend to explore such scenarios on a case by case basis in a future work.

We also briefly discuss the collider implications of jet matched signal samples. In the analysis presented in Sec. II,

we used the jet matched background samples while the signal samples were generated without any jet matching. The underlying reason is the negligible difference in the kinematic features of the final state particles of the signal produced with and without jet matching. In Figs. 11 and 12, we illustrate the p_T and η distributions, respectively, of the χ_1^0's with the highest and second highest p_T produced via $pp \to (\chi_2^0 \to \chi_1^0 W^\pm)(\tilde{\chi}_1^\pm \to \chi_1^0 Z)$, at the HL-LHC. The blue dashed line corresponds to the 0 jet matched sample while the black dot-dashed and red dot-dot-dashed lines represent the distributions for 1 jet and 2 jet matched samples. These distributions indicate that jet matching has almost a negligible effect on the final state kinematics and it is safe to consider the 0 jet matched signal samples only.

In this work, we have used the traditional cut-based analysis to discriminate the signal from the background. It would be important and interesting to gauge the benefits of employing advanced analysis techniques like jet substructure to perform the signal-background discrimination. Before concluding this paper, we intend to briefly discuss this aspect as well. In order to study the study the prospects of jet substructure techniques, we consider two
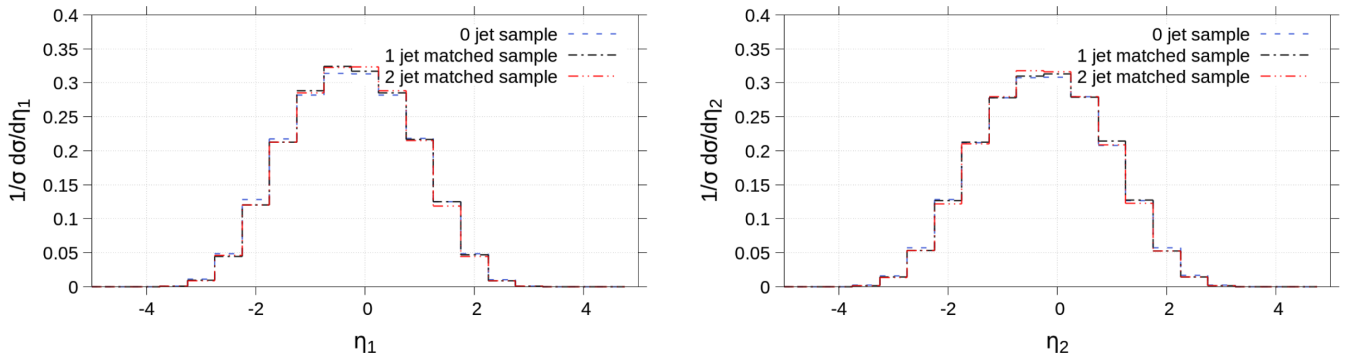

FIG. 12.   Normalized distributions illustrating the η of the χ_1^0's produced via $pp \to \chi_1^\pm \chi_2^0 \to (W^\pm \chi_1^0)(Z\chi_1^0)$ at the HL-LHC. η_1 (left panel) and η_2 (right panel) represent the pseudorapidity of the χ_1^0 with the highest and second highest p_T. The distributions correspond to 2 jet (red dot-dashed line), 1 jet (black dot-dashed line) and 0 jet matched (blue dashed line) samples.
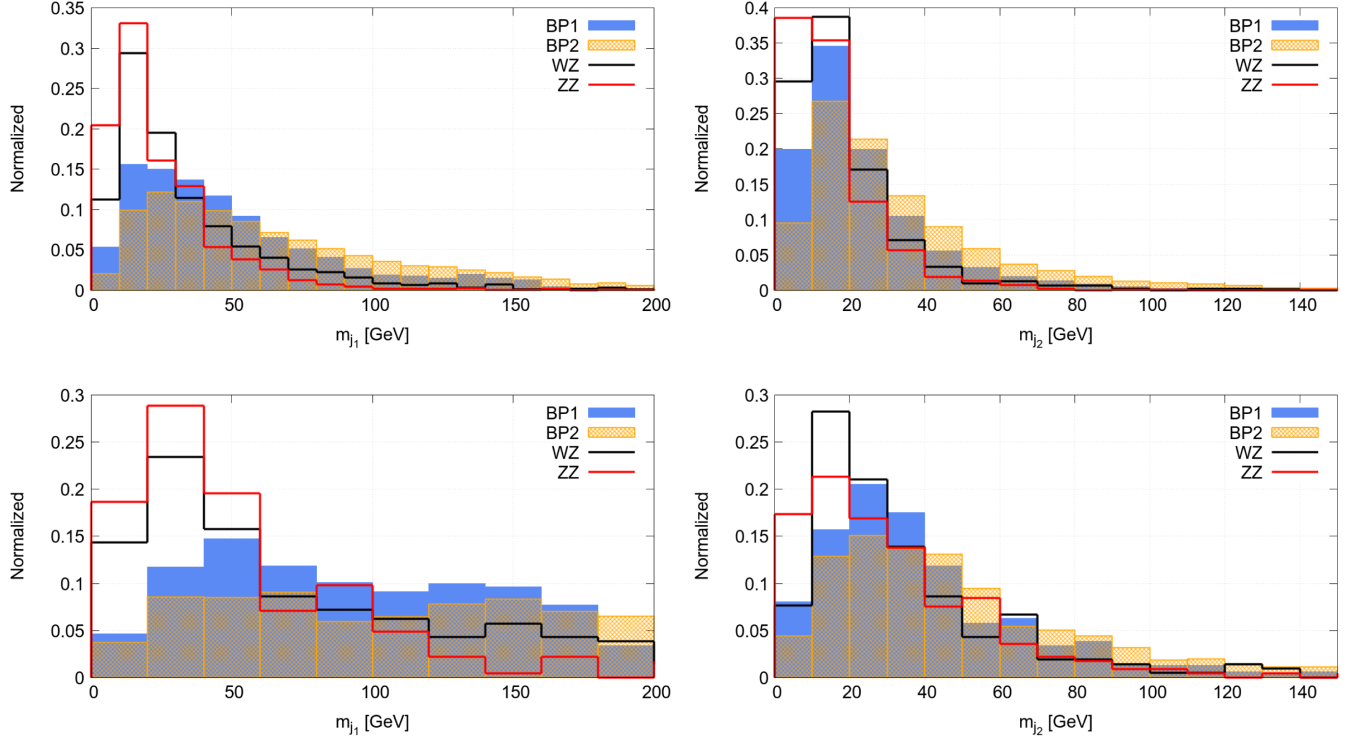
FIG. 13.   Top panel: Normalized distributions illustrating the invariant mass of j_1 (m_{j_1}) and j_2 (m_{j_2}), reconstructed with $R = 0.8$, for BP-J1 (blue shaded region), BP-J2 (orange shaded region), WZ + jets (black solid line) and ZZ + jets (red solid line), in the left and right panels, respectively. Bottom panel: Same as the top panel, but with jets reconstructed with $R = 1.5$.

signal benchmark points: BP-J1 ($M_{\chi_1^\pm, \chi_2^0} = 350$ GeV, $M_{\chi_1^0} = 150$ GeV) and BP-J2 ($M_{\chi_1^\pm, \chi_2^0} = 550$ GeV, $M_{\chi_1^0} = 300$ GeV), and simulate the signal process: $pp \to \chi_1^\pm \chi_2^0 \to (W^\pm \chi_1^0) \times (Z\chi_1^0) \to (W \to l'\nu)(\chi_1^0 \to \text{jets})(Z \to l'l')(\chi_1^0 \to \text{jets}) \to 3l + \text{jets} + \not{E}_T$. The relevant background processes are $WZ + $ jets and $ZZ + $ jets. In order to study the prospects of jet substructure techniques, we modify the anti-k_t jet reconstruction definition by choosing a relatively large jet radius parameter (R). In this regard, we choose two different values of R, 0.8 and 1.5. We intend to investigate the internal structure of the reconstructed jets and their p_T distributions for both, signal and background, in order to understand the merit of using the jet substructure for signal-background discrimination. Our basic event selection

criteria demands at least 2 jets and 3 leptons (electrons or muons) in the final state. The invariant mass distribution of the leading and subleading p_T ordered jets (represented as j_1 and j_2, respectively) would provide a window to the internal structure of the jets. We illustrate the invariant mass of j_1 and j_2, reconstructed with $R = 0.8$, in Fig. 13 (top left panel) and (top right panel), respectively. The invariant mass distribution for j_1 and j_2 reconstructed with $R = 1.5$ are also shown in the bottom left panel and the bottom right panel, respectively, of the same figure.

It is observed from Fig. 13 that the signal benchmark points do not display any significant difference or any distinct kinematic features from the background processes for both $R = 0.8$ and $R = 1.5$. Choosing a larger jet radius parameter makes the jet invariant distributions flatter and

TABLE VII.   Table illustrating the fraction of events (after passing the selection cuts: $N_j \geq 2$, $N_l = 3$, $N_b = 0$) with p_{T,j_i} ($j = 1, 2$) above $2M_{\chi_1^0}$, $2M_Z$ and $2M_{W^\pm}$.

$(M_{\chi_1^0}, M_{\chi_2^0, \chi_1^\pm})$		$R = 0.8$			$R = 1.5$		
	p_T	$> 2M_{\chi_1^0}$	$> 2M_Z$	$> 2M_W$	$> 2M_{\chi_1^0}$	$> 2M_Z$	$> 2M_W$
BP1	j_1	0.16	0.46	0.56	0.12	0.46	0.54
(150 GeV, 350 GeV)	j_2	0.02	0.11	0.15	6×10^{-3}	0.06	0.07
BP1	j_1	0.06	0.8	0.86	0.03	0.75	0.8
(300 GeV, 550 GeV)	j_2	5×10^{-3}	0.35	0.45	8×10^{-4}	0.19	0.26

the peak slightly shifts to a higher value. We also identified the fraction of events with a large $p_{T.j_{1,2}}$ i.e., above $2M_{\chi_1^0}$, $2M_Z$ and $2M_W$. The results have been displayed in Table VII. We observe that the fraction of events with $p_{T.j_1}$ above the $2M_{\chi_1^0}$ threshold is $\sim 16\%$ and $\sim 12\%$ for BP-J1 with $R = 0.8$ and $R = 1.5$, respectively. In the case of BP-J2, where the χ_1^0 is much heavier, the corresponding fraction of events are further small, $\sim 6\%$ and $\sim 3\%$, respectively. It can be concluded from these discussions that jet substructure techniques might help in improving the signal-background discrimination to some extent, however, gaining a thorough understanding of the improvement warrants a detailed analysis of its own which is beyond the scope of this paper.

We conclude our discussions here and proceed to provide a detailed summary and conclusion to our results.

IV. SUMMARY AND CONCLUSIONS

In this work, we studied the sensitivity of the future HL-LHC to direct wino searches in a simplified scenario with $\lambda_{112}'' u^c d^c s^c$- and $\lambda_{113}'' u^c d^c b^c$-type RPV operators. The collider implications of $\lambda_{112}'' u^c d^c s^c$-type RPV coupling on direct wino searches in the Wh mediated $1l + 2b + \text{jets}(N_j \gtrsim 2) + \not{E}_T$, Wh mediated $1l + 2\gamma + \text{jets}(N_j \gtrsim 2) + \not{E}_T$ and WZ mediated $3l + \text{jets}(N_j \gtrsim 2) + \not{E}_T$ has been studied in Sec. II A, II B and II C, respectively, while Sec. II D examined the projected reach of direct wino searches in the WZ mediated $3l + 2b + \text{jets}(N_j \gtrsim 2) + \not{E}_T$ final state, by the virtue of $\lambda_{113}'' u^c d^c b^c$-type RPV operator. The direct production of mass degenerate wino type $\chi_1^\pm \chi_2^0$ was considered which eventually underwent cascade decay into bino type χ_1^0 along with the h, W and/or Z bosons. In the presence of $\lambda_{u^c d^c s^c (b^c)}''$-type RPV operator, the χ_1^0 decays into $\chi_1^0 \to uds$ ($\chi_1^0 \to udb$) resulting in jets in the final state.

A detailed collider analysis was performed in the aforesaid channels by taking into account all relevant background samples and by considering a multitude of important kinematic variables. Direct wino searches in the Wh mediated $1l + 2b + \text{jets} + \not{E}_T$ final state in the context of $\lambda'' u^c d^c s^c$-type RPV scenario exhibited a projected 2σ exclusion (5σ discovery) reach up to $M_{\chi_1^\pm \chi_2^0} \sim 680$ GeV (~ 450 GeV) for a binolike χ_1^0 with mass up to ~ 0 GeV. It is to be noted that the respective reinterpretation within a RPC scenario (studied in [153]) furnishes considerably stringent projections, and the respective 95% C.L. projected exclusion contour reaches up to $M_{\chi_1^\pm \chi_2^0}$ up to ~ 1100 GeV for binolike χ_1^0 with mass $M_{\chi_1^0} \sim 0$ GeV. The same simplified RPV scenario was also interpreted in terms of searches in the Wh mediated $1l + 2\gamma + \text{jets} + \not{E}_T$ final state, and a relatively stronger potential reach was observed. Here, the projected exclusion and discovery

contours had reached up to ~ 700 and ~ 600 GeV, respectively.

As discussed previously in Sec. II C, the future reach of direct wino searches in the WZ mediated $3l + \not{E}_T$ final state within a RPC framework has been studied in [153], and the projected 95% C.L. exclusion contour reaches up to ~ 1150 GeV for a binolike χ_1^0 with mass up to ~ 0 GeV. We performed a collider study to derive the projected reach of direct wino searches in the WZ mediated $3l + \text{jets} + \not{E}_T$ final state and reinterpreted the projected reach within a $\lambda_{112}'' u^c d^c s^c$-type RPV scenario. The projected exclusion and discovery contours displayed a considerably weaker reach as compared to the RPC scenario [153]. The projected 2σ exclusion contour reached up to ~ 660 GeV while the projected 5σ discovery contour reached up to ~ 490 GeV. Similarly, in Sec. II D, the projected reach of direct wino searches in the WZ mediated $3l + 2b + \text{jets} + \not{E}_T$ final state was reinterpreted to simplified scenario with $\lambda_{113}'' u^c d^c b^c$-type RPV coupling. The projected exclusion reach of this search channel reaches up to ~ 600 GeV for $M_{\chi_1^0}$ in between ~ 150 and ~ 250 GeV.

A few benchmark scenarios have been explored in Sec. III. The future reach of direct higgsino production at the HL-LHC in the aforesaid channels was analyzed for BP-$\alpha_{\tilde{H}}$ and BP-$\beta_{\tilde{H}}$. It is observed that the direct higgsino searches furnish weaker projection contours compared to the wino counterparts due to a smaller production rate. Furthermore, the sensitivity of the analysis channels to $\tan\beta$ is also studied. The WZ mediated channels displayed an improvement in signal significance with an increase in $\tan\beta$, with all other MSSM input parameters kept fixed. The implications of a finite wino-higgsino mixing in the heavier ino states on the projected reach of the search channels considered in this work is also analyzed for the case of BP-$\beta_{\tilde{W}}^{10}$, BP-$\beta_{\tilde{W}}^{30}$, BP-$\beta_{\tilde{W}}^{50}$ and BP-$\beta_{\tilde{W}}^{70}$. These benchmark points resulted in a combined signal significance of $2.01, 1.98, 2.33$ and 2.12, respectively, thereby, marginally falling within the projected exclusion reach (except for BP-$\beta_{\tilde{W}}^{30}$) of HL-LHC. Towards the end, we also briefly discuss the prospects of using jet substructure to improve the signal-background discrimination.

ACKNOWLEDGMENTS

APPENDIX: SIGNAL AND BACKGROUND CROSS SECTIONS

TABLE VIII. The cross section of the signal benchmark points and the background processes are shown. The signal cross sections are at NLO-NLL order (taken from [159,160]). For the background processes, the LO cross section values computed by MadGraph_aMC@NLO have been considered with the exception of $t\bar{t}$ + jets for which the NLO cross section is considered (the NLO cross section has been obtained by multiplying the LO cross section with the k factor ($k \simeq 1.5$).)

Final State		Process	Cross Section (fb)
Wh mediated $1l + 2b$ + jets + $\not{E}_T$ (Sec. II A)	Signal benchmark points	BP1-A ($M_{\chi_2^0} = 200$ GeV, $M_{\chi_1^0} = 55$ GeV)	381
		BP1-B ($M_{\chi_2^0} = 350$ GeV, $M_{\chi_1^0} = 165$ GeV)	46
		BP1-C ($M_{\chi_2^0} = 500$ GeV, $M_{\chi_1^0} = 25$ GeV)	10
	Background	$t\bar{t}$ + jets	9.15×10^5
		WW + jets	8.92×10^4
		WZ + jets	4.01×10^4
		ZZ + jets	1.17×10^4
		Wh + jets ($h \to b\bar{b}, W \to l'\nu$)	334
		Zh + jets ($h \to b\bar{b}, Z \to l'l'$)	54
Wh mediated $1l + 2\gamma$ + jets (Sec. II B)	Signal benchmark points	BP2-A ($M_{\chi_2^0} = 250$ GeV, $M_{\chi_1^0} = 100$ GeV)	0.67
		BP2-B ($M_{\chi_2^0} = 425$ GeV, $M_{\chi_1^0} = 100$ GeV)	0.08
		BP2-C ($M_{\chi_2^0} = 600$ GeV, $M_{\chi_1^0} = 150$ GeV)	0.02
	Background	$t\bar{t}h$ + jets($h \to \gamma\gamma$)	0.82
		Wh + jets($h \to \gamma\gamma, W \to l'\nu$)	0.61
		Zh + jets($h \to \gamma\gamma, Z \to l'l'$)	0.10
WZ mediated $3l$ + jets + $\not{E}_T$ (Sec. II C)	Signal benchmark points	BP3-A ($M_{\chi_2^0} = 400$ GeV, $M_{\chi_1^0} = 175$ GeV)	4.71
		BP3-B ($M_{\chi_2^0} = 600$ GeV, $M_{\chi_1^0} = 325$ GeV)	0.82
		BP3-C ($M_{\chi_2^0} = 650$ GeV, $M_{\chi_1^0} = 175$ GeV)	0.56
	Background	WZ + jets	40080
		ZZ + jets	11690
		VVV + jets	799
WZ mediated $3l + 2b$ + jets + $\not{E}_T$ (Sec. II D)	Signal benchmark points	BP4-A ($M_{\chi_2^0} = 250$ GeV, $M_{\chi_1^0} = 135$ GeV)	29
		BP4-B ($M_{\chi_2^0} = 600$ GeV, $M_{\chi_1^0} = 205$ GeV)	0.8
		BP4-C ($M_{\chi_2^0} = 700$ GeV, $M_{\chi_1^0} = 85$ GeV)	0.4
	Background	$t\bar{t}Z$	762
		VVV + jets	1037
		WZ + jets ($W \to l'\nu, Z \to l'l'$)	248
		ZZ + jets ($Z \to l'l', Z \to l'l'$)	319

[1] J. Wess and B. Zumino, Supergauge transformations in four dimensions, Nucl. Phys. **B70**, 39 (1974).

[2] H. Nilles, Supersymmetry, supergravity and particle physics, Phys. Rep. **110**, 1 (1984).

[3] H. E. Haber and G. L. Kane, The search for supersymmetry: Probing physics beyond the Standard Model, Phys. Rep. **117**, 75 (1985).

[4] H. P. Nilles, Supersymmetry, supergravity and particle physics, Phys. Rep. **110**, 1 (1984).

[5] S. L. Glashow, Partial-symmetries of weak interactions, Nucl. Phys. **22**, 579 (1961).

[6] S. Weinberg, A Model of Leptons, Phys. Rev. Lett. **19**, 1264 (1967).

[7] A. Salam, Weak and electromagnetic interactions, Conf. Proc. C **680519**, 367 (1968).

[8] M. Gell-Mann, A schematic model of baryons and mesons, Phys. Lett. **8**, 214 (1964).

[9] E. Gildener Gauge-symmetry hierarchies, Phys. Rev. D **14**, 1667 (1976).

[10] M. J. G. Veltman, The infrared—ultraviolet connection, Acta Phys. Pol. B **12**, 437 (1981).

[11] J. Ellis, S. Kelley, and D. Nanopoulos, Precision LEP data, supersymmetric guts and string unification, Phys. Lett. B **249**, 441 (1990).

[12] U. Amaldi, W. de Boer, and H. Furstenau, Comparison of grand unified theories with electroweak and strong

coupling constants measured at LEP, Phys. Lett. B **260,** 447 (1991).

[13] G. G. Ross and R. G. Roberts, Minimal supersymmetric unification predictions, Nucl. Phys. **B377,** 571 (1992).

[14] C. Giunti, C. W. Kim, and U. W. Lee, Running coupling constants and grand unification models, Mod. Phys. Lett. A **06,** 1745 (1991).

[15] F. Zwicky, Die Rotverschiebung von extragalaktischen Nebeln, Helv. Phys. Acta **6,** 110 (1933).

[16] F. Zwicky, On the masses of nebulae and of clusters of nebulae, Astrophys. J. **86,** 217 (1937).

[17] Y. Sofue and V. Rubin, Rotation curves of spiral galaxies, Annu. Rev. Astron. Astrophys. **39,** 137 (2001).

[18] L. Susskind, Dynamics of spontaneous symmetry breaking in the weinberg-salam theory, Phys. Rev. D **20,** 2619 (1979).

[19] L. Susskind, The gauge hierarchy problem, technicolor, supersymmetry, and all that, Phys. Rep. **104,** 181 (1984).

[20] S. P. Martin, A Supersymmetry primer, Adv. Ser. Dir. High Energy Phys. **21,** 1 (2010); **18,** 1 (1998).

[21] I. Aitchison, *Supersymmetry in Particle Physics: An Elementary Introduction* (Cambridge University Press, Cambridge, England, 2007).

[22] A. Djouadi, The anatomy of electro-weak symmetry breaking. II. The Higgs bosons in the minimal supersymmetric model, Phys. Rep. **459,** 1 (2008).

[23] H. Baer and X. Tata, *Weak scale supersymmetry: From Superfields to Scattering Events* (Cambridge University Press, Cambridge, England, 2006).

[24] M. Drees, R. Godbole, and P. Roy, Theory and phenomenology of sparticles: An account of four-dimensional $N = 1$ supersymmetry in high energy physics (World Scientific, Singapore, 2004).

[25] M. Carena, S. Gori, N. R. Shah, and C. E. M. Wagner, A 125 GeV SM-like Higgs in the MSSM and the $\gamma\gamma$ rate, J. High Energy Phys. 03 (2012) 014.

[26] A. Arbey, M. Battaglia, A. Djouadi, F. Mahmoudi, and J. Quevillon, Implications of a 125 GeV Higgs for supersymmetric models, Phys. Lett. B **708,** 162 (2012).

[27] H. Baer, V. Barger, P. Huang, D. Mickelson, A. Mustafayev, and X. Tata, Post-LHC7 fine-tuning in the minimal supergravity/CMSSM model with a 125 GeV Higgs boson, Phys. Rev. D **87,** 035017 (2013).

[28] A. Arbey, M. Battaglia, A. Djouadi, and F. Mahmoudi, The Higgs sector of the phenomenological MSSM in the light of the Higgs boson discovery, J. High Energy Phys. 09 (2012) 107.

[29] W. Altmannshofer, M. Carena, N. R. Shah, and F. Yu, Indirect probes of the MSSM after the Higgs discovery, J. High Energy Phys. 01 (2013) 160.

[30] P. Bechtle, S. Heinemeyer, O. Stal, T. Stefaniak, G. Weiglein, and L. Zeune, MSSM interpretations of the LHC discovery: Light or heavy Higgs?, Eur. Phys. J. C **73,** 2354 (2013).

[31] A. Djouadi, Implications of the Higgs discovery for the MSSM, Eur. Phys. J. C **74,** 2704 (2014).

[32] K. Cheung, J. S. Lee, and P.-Y. Tseng, Higgs precision (Higgcision) Era begins, J. High Energy Phys. 05 (2013) 134.

[33] A. Ahmadov and M. Demirci, Single neutralino production at the LHC, Phys. Rev. D **88,** 015017 (2013).

[34] J. Chakrabortty, A. Choudhury, and S. Mondal, Non-universal Gaugino mass models under the lamppost of muon (g-2), J. High Energy Phys. 07 (2015) 038.

[35] K. Kowalska, L. Roszkowski, E. M. Sessolo, and A. J. Williams, GUT-inspired SUSY and the muon g-2 anomaly: Prospects for LHC 14 TeV, J. High Energy Phys. 06 (2015) 020.

[36] D. Chowdhury and O. Eberhardt, Global fits of the two-loop renormalized Two-Higgs-Doublet model with soft Z_2 breaking, J. High Energy Phys. 11 (2015) 052.

[37] B. Bhattacherjee, A. Chakraborty, and A. Choudhury, Status of the MSSM Higgs sector using global analysis and direct search bounds, and future prospects at the High Luminosity LHC, Phys. Rev. D **92,** 093007 (2015).

[38] P. Bechtle, S. Heinemeyer, O. Stal, T. Stefaniak, and G. Weiglein, Applying exclusion likelihoods from LHC searches to extended Higgs sectors, Eur. Phys. J. C **75,** 421 (2015).

[39] R. K. Barman, B. Bhattacherjee, A. Choudhury, D. Chowdhury, J. Lahiri, and S. Ray, Current status of MSSM Higgs sector with LHC 13 TeV data, Eur. Phys. J. Plus **134,** 150 (2019).

[40] A. Barr and J. Liu, Analysing parameter space correlations of recent 13 TeV gluino and squark searches in the pMSSM, Eur. Phys. J. C **77,** 202 (2017).

[41] K. Kowalska, Phenomenological MSSM in light of new 13 TeV LHC data, Eur. Phys. J. C **76,** 684 (2016).

[42] C. Han, J. Ren, L. Wu, J. M. Yang, and M. Zhang, Top-squark in natural SUSY under current LHC run-2 data, Eur. Phys. J. C **77,** 93 (2017).

[43] M. R. Buckley, D. Feld, S. Macaluso, A. Monteux, and D. Shih, Cornering natural SUSY at LHC Run II and beyond, J. High Energy Phys. 08 (2017) 115.

[44] A. Choudhury, L. Darme, L. Roszkowski, E. M. Sessolo, and S. Trojanowski, Muon g—2 and related phenomenology in constrained vector-like extensions of the MSSM, J. High Energy Phys. 05 (2017) 072.

[45] J. Zhao, The Higgs properties in the MSSM after the LHC Run-2, Int. J. Mod. Phys. A **33,** 1841001 (2018).

[46] P. Athron *et al.* (GAMBIT Collaboration), A global fit of the MSSM with GAMBIT, Eur. Phys. J. C **77,** 879 (2017).

[47] E. Bagnaschi *et al.*, Likelihood analysis of the pMSSM11 in light of LHC 13-TeV data, Eur. Phys. J. C **78,** 256 (2018).

[48] J. C. E. A. Costa, Likelihood analysis of the sub-gut mssm in light of LHC 13-tev data, Eur. Phys. J. C **78,** 158 (2018).

[49] H. M. Tran and H. T. Nguyen, GUT-inspired MSSM in light of muon $g - 2$ and LHC results at $\sqrt{s} = 13$ TeV, Phys. Rev. D **99,** 035040 (2019).

[50] M. Endo, K. Hamaguchi, S. Iwamoto, and T. Kitahara, Muon g-2 vs LHC Run 2 in supersymmetric models, J. High Energy Phys. 04 (2020) 165.

[51] CMS Collaboration, Search for supersymmetry in proton-proton collisions at 13 TeV in final states with jets and missing transverse momentum, Technical Report No. CMS-PAS-SUS-19-006, CERN, Geneva, 2019, http://cds.cern.ch/record/2682103.

[52] CMS Collaboration, Search for supersymmetry in pp collisions at $\sqrt{s} = 13$ TeV with 137 fb^{-1} in the final state with a single lepton using the sum of masses of large-radius jets, Technical Report No. CMS-PAS-SUS-19-007, CERN, Geneva, 2019, http://cds.cern.ch/record/2685097.

[53] ATLAS Collaboration, Search for squarks and gluinos in final states with jets and missing transverse momentum using 139 fb^{-1} of $\sqrt{s} = 13$ TeV pp collision data with the ATLAS detector, Technical Report No. ATLAS-CONF-2019-040, CERN, Geneva, 2019, https://cds.cern.ch/record/2686254.

[54] CMS Collaboration, Searches for new phenomena in events with jets and high values of the M_{T2} variable, including signatures with disappearing tracks, in proton-proton collisions at $\sqrt{s} = 13$ TeV, Technical Report No. CMS-PAS-SUS-19-005, CERN, Geneva, 2019, http://cds.cern.ch/record/2668105.

[55] CMS Collaboration, Search for direct top squark pair production in events with one lepton, jets and missing transverse energy at 13 TeV, Technical Report No. CMS-PAS-SUS-19-009, CERN, Geneva, 2019, http://cds.cern.ch/record/2682157.

[56] A. M. Sirunyan *et al.* (CMS Collaboration), Search for electroweak production of charginos and neutralinos in WH events in proton-proton collisions at $\sqrt{s} = 13$ TeV, J. High Energy Phys. 11 (2017) 029.

[57] CMS Collaboration, Search for supersymmetry with a compressed mass spectrum in events with a soft τ lepton, a highly energetic jet, and large missing transverse momentum in proton-proton collisions at $\sqrt{s} = 13$ TeV, Technical Report No. CMS-PAS-SUS-19-002, CERN, Geneva, 2019, http://cds.cern.ch/record/2684821.

[58] CMS Collaboration, Search for supersymmetry using Higgs boson to diphoton decays at $\sqrt{s} = 13$ TeV with the CMS detector, Technical Report No. CMS-PAS-SUS-18-007, CERN, Geneva, 2019, https://cds.cern.ch/record/2675233.

[59] A. M. Sirunyan *et al.* (CMS Collaboration), Combined search for electroweak production of charginos and neutralinos in proton-proton collisions at $\sqrt{s} = 13$ TeV, J. High Energy Phys. 03 (2018) 160.

[60] G. Aad *et al.* (ATLAS Collaboration), Searches for electroweak production of supersymmetric particles with compressed mass spectra in $\sqrt{s} = 13$ TeV pp collisions with the ATLAS detector, Phys. Rev. D **101**, 052005 (2020).

[61] G. Aad *et al.* (ATLAS Collaboration), Search for chargino-neutralino production with mass splittings near the electroweak scale in three-lepton final states in $\sqrt{s} = 13$ TeV pp collisions with the ATLAS detector, Phys. Rev. D **101**, 072001 (2020).

[62] G. Aad *et al.* (ATLAS Collaboration), Search for direct production of electroweakinos in final states with one lepton, missing transverse momentum and a Higgs boson decaying into two b-jets in (pp) collisions at $\sqrt{s} = 13$ TeV with the ATLAS detector, Eur. Phys. J. C **80**, 691 (2020).

[63] M. Chakraborti, U. Chattopadhyay, A. Choudhury, A. Datta, and S. Poddar, The electroweak sector of the pMSSM in the light of LHC—8 TeV and other data, J. High Energy Phys. 07 (2014) 019.

[64] S. P. Das, M. Guchait, and D. P. Roy, Testing SUSY models for the muon $g - 2$ anomaly via chargino-neutralino pair production at the LHC, Phys. Rev. D **90**, 055011 (2014).

[65] M. Chakraborti, U. Chattopadhyay, A. Choudhury, A. Datta, and S. Poddar, Reduced LHC constraints for higgsino-like heavier electroweakinos, J. High Energy Phys. 11 (2015) 050.

[66] A. Choudhury and S. Mondal, Revisiting the exclusion limits from direct chargino-neutralino production at the LHC, Phys. Rev. D **94**, 055024 (2016).

[67] M. Chakraborti, A. Datta, N. Ganguly, and S. Poddar, Multilepton signals of heavier electroweakinos at the LHC, J. High Energy Phys. 11 (2017) 117.

[68] G. Pozzo and Y. Zhang, Constraining resonant dark matter with combined LHC electroweakino searches, Phys. Lett. B **789**, 582 (2019).

[69] A. Datta and N. Ganguly, The past, present and future of the heavier electroweakinos in the light of LHC and other data, J. High Energy Phys. 01 (2019) 103.

[70] D. Hooper and T. Plehn, Supersymmetric dark matter: How light can the LSP be?, Phys. Lett. B **562**, 18 (2003).

[71] N. Bhattacharyya, A. Choudhury, and A. Datta, Low mass neutralino dark matter in mSUGRA and more general models in the light of LHC data, Phys. Rev. D **84**, 095006 (2011).

[72] D. A. Vasquez, G. Belanger, and C. Boehm, Revisiting light neutralino scenarios in the MSSM, Phys. Rev. D **84**, 095015 (2011).

[73] A. Choudhury and A. Datta, Many faces of low mass neutralino dark matter in the unconstrained MSSM, LHC data and new signals, J. High Energy Phys. 06 (2012) 006.

[74] A. Fowlie, K. Kowalska, L. Roszkowski, E. M. Sessolo, and Y.-L. S. Tsai, Dark matter and collider signatures of the MSSM, Phys. Rev. D **88**, 055012 (2013).

[75] L. Roszkowski, E. M. Sessolo, and A. J. Williams, Prospects for dark matter searches in the pMSSM, J. High Energy Phys. 02 (2015) 014.

[76] K. Hamaguchi and K. Ishikawa, Prospects for Higgs- and Z-resonant neutralino dark matter, Phys. Rev. D **93**, 055009 (2016).

[77] T. Han, Z. Liu, and S. Su, Light neutralino dark matter: Direct/Indirect detection and collider searches, J. High Energy Phys. 08 (2014) 093.

[78] G. Blanger, G. D. La Rochelle, B. Dumont, R. M. Godbole, S. Kraml, and S. Kulkarni, LHC constraints on light neutralino dark matter in the MSSM, Phys. Lett. B **726**, 773 (2013).

[79] B. Ananthanarayan, J. Lahiri, P. N. Pandita, and M. Patra, Invisible decays of the lightest Higgs boson in supersymmetric models, Phys. Rev. D **87**, 115021 (2013).

[80] H. K. Dreiner, J. S. Kim, and O. Lebedev, First LHC constraints on neutralinos, Phys. Lett. B **715**, 199 (2012).

[81] A. Choudhury and A. Datta, Neutralino dark matter confronted by the LHC constraints on electroweak SUSY signals, J. High Energy Phys. 09 (2013) 119.

[82] L. Calibbi, T. Ota, and Y. Takanishi, Light Neutralino in the MSSM: A playground for dark matter, flavor physics and collider experiments, J. High Energy Phys. 07 (2011) 013.

[83] G. Belanger, F. Boudjema, A. Cottrant, A. Pukhov, and S. Rosier-Lees, Lower limit on the neutralino mass in the general MSSM, J. High Energy Phys. 03 (2004) 012.

[84] G. Belanger, F. Boudjema, A. Cottrant, R. M. Godbole, and A. Semenov, The MSSM invisible Higgs in the light of dark matter and g-2, Phys. Lett. B **519,** 93 (2001).

[85] G. Belanger, F. Boudjema, F. Donato, R. Godbole, and S. Rosier-Lees, SUSY Higgs at the LHC: Effects of light charginos and neutralinos, Nucl. Phys. **B581,** 3 (2000).

[86] R. K. Barman, G. Belanger, B. Bhattacherjee, R. Godbole, G. Mendiratta, and D. Sengupta, Invisible decay of the Higgs boson in the context of a thermal and nonthermal relic in MSSM, Phys. Rev. D **95,** 095018 (2017).

[87] M. Chakraborti, U. Chattopadhyay, and S. Poddar, How light a higgsino or a wino dark matter can become in a compressed scenario of MSSM, J. High Energy Phys. 09 (2017) 064.

[88] I. Hinchliffe and T. Kaeding, *b*- and *l*-violating couplings in the minimal supersymmetric Standard Model, Phys. Rev. D **47,** 279 (1993).

[89] G. Bhattacharyya and P. B. Pal, New constraints on R-parity violation from proton stability, Phys. Lett. B **439,** 81 (1998).

[90] L. E. Ibanez and G. G. Ross, Discrete gauge symmetry anomalies, Phys. Lett. B **260,** 291 (1991).

[91] H. K. Dreiner, C. Luhn, and M. Thormeier, What is the discrete gauge symmetry of the MSSM?, Phys. Rev. D **73,** 075007 (2006).

[92] H. K. Dreiner, C. Luhn, H. Murayama, and M. Thormeier, Baryon triality and neutrino masses from an anomalous flavor U(1), Nucl. Phys. **B774,** 127 (2007).

[93] H. K. Dreiner, M. Hanussek, and C. Luhn, What is the discrete gauge symmetry of the R-parity violating MSSM?, Phys. Rev. D **86,** 055012 (2012).

[94] H. K. Dreiner, An Introduction to explicit R-parity violation, Adv. Ser. Dir. High Energy Phys. **21,** 565 (2010).

[95] R. Barbier *et al.*, R-parity violating supersymmetry, Phys. Rep. **420,** 1 (2005).

[96] E. J. Chun and H. B. Kim, Nonthermal axino as cool dark matter in supersymmetric standard model without R-parity, Phys. Rev. D **60,** 095006 (1999).

[97] E. J. Chun and H. B. Kim, Axino light dark matter and neutrino masses with R-parity violation, J. High Energy Phys. 10 (2006) 082.

[98] F. Takayama and M. Yamaguchi, Gravitino dark matter without R-parity, Phys. Lett. B **485,** 388 (2000).

[99] H. K. Dreiner, K. Nickel, and F. Staub, On the two-loop corrections to the Higgs mass in trilinear R-parity violation, Phys. Lett. B **742,** 261 (2015).

[100] B. Bhattacherjee, J. L. Evans, M. Ibe, S. Matsumoto, and T. T. Yanagida, Natural supersymmetry's last hope: R-parity violation via UDD operators, Phys. Rev. D **87,** 115002 (2013).

[101] M. Asano, K. Sakurai, and T. T. Yanagida, Multi-hadron final states in RPV supersymmetric models with extra matter, Phys. Lett. B **736,** 356 (2014).

[102] ATLAS Collaboration, Search for massive supersymmetric particles in multi-jet final states produced in pp collisions at $\sqrt{s} = 13$ TeV using the ATLAS detector at the LHC, Technical Report No. ATLAS-CONF-2016-057, CERN, Geneva, 2016, https://cds.cern.ch/record/2206149.

[103] A. M. Sirunyan *et al.* (CMS Collaboration), Search for R-parity violating supersymmetry in pp collisions at $\sqrt{s} = 13$ TeV using b jets in a final state with a single lepton, many jets, and high sum of large-radius jet masses, Phys. Lett. B **783,** 114 (2018).

[104] M. Aaboud *et al.* (ATLAS Collaboration), Search for R-parity-violating supersymmetric particles in multi-jet final states produced in *p-p* collisions at $\sqrt{s} = 13$ TeV using the ATLAS detector at the LHC, Phys. Lett. B **785,** 136 (2018).

[105] P. W. Graham, S. Rajendran, and P. Saraswat, Supersymmetric crevices: Missing signatures of R-parity violation at the LHC, Phys. Rev. D **90,** 075005 (2014).

[106] CMS Collaboration, Search for low-mass pair-produced dijet resonances using jet substructure techniques in proton-proton collisions at a center-of-mass energy of $\sqrt{s} = 13$ TeV, Technical Report No. CMS-PAS-EXO-16-029, CERN, Geneva, 2016, https://cds.cern.ch/record/2231062.

[107] L. J. Hall and M. Suzuki, Explicit R-parity breaking in supersymmetric models, Nucl. Phys. **B231,** 419 (1984).

[108] B. Mukhopadhyaya, Neutrino mass patterns, R-parity violating supersymmetry and associated phenomenology, Pramana **54,** 147 (2000).

[109] O. C. W. Kong, On the formulation of the generic supersymmetric standard model (or supersymmetry without R parity), Int. J. Mod. Phys. A **19,** 1863 (2004).

[110] S. Rakshit, Neutrino masses and R-parity violation, Mod. Phys. Lett. A **19,** 2239 (2004).

[111] P. Dey, A. Kundu, B. Mukhopadhyaya, and S. Nandi, Two-loop neutrino masses with large R-parity violating interactions in supersymmetry, J. High Energy Phys. 12 (2008) 100.

[112] A. Datta and S. Poddar, Probing R-parity violating models of neutrino mass at the LHC via top squark decays, Phys. Rev. D **79,** 075021 (2009).

[113] R. Bose, A. Datta, A. Kundu, and S. Poddar, LHC signatures of neutrino mass generation through R-parity violation, Phys. Rev. D **90,** 035007 (2014).

[114] A. Datta, R. Gandhi, B. Mukhopadhyaya, and P. Mehta, Signals of R-parity violating supersymmetry in neutrino scattering at muon storage rings, Phys. Rev. D **64,** 015011 (2001).

[115] A. Chakraborty and S. Chakraborty, Probing $(g-2)_\mu$ at the LHC in the paradigm of R-parity violating MSSM, Phys. Rev. D **93,** 075035 (2016).

[116] D. Bardhan, A. Chakraborty, D. Choudhury, D. K. Ghosh, and M. Maity, Search for bottom squarks in the baryon-number violating MSSM, Phys. Rev. D **96,** 035024 (2017).

[117] J. Guo, J. Li, T. Li, F. Xu, and W. Zhang, Deep learning for R-parity violating supersymmetry searches at the LHC, Phys. Rev. D **98,** 076017 (2018).

[118] R. N. Mohapatra, Supersymmetry and R-parity: An overview, Phys. Scr. **90,** 088004 (2015).

[119] F. Domingo, H. K. Dreiner, J. S. Kim, M. E. Krauss, V. M. Lozano, and Z. S. Wang, Updating bounds on R-parity violating supersymmetry from meson oscillation data, J. High Energy Phys. 02 (2019) 66.

[120] M. E. Aaboud (ATLAS Collaboration), Search for super-symmetry in events with four or more leptons in $\sqrt{s} =$ 13 TeV pp collisions with atlas, Phys. Rev. D **98,** 032009 (2018).

[121] G. Aad *et al.* (ATLAS Collaboration), Search for super-symmetry in events with four or more leptons in $\sqrt{s} =$ 8 TeV pp collisions with the ATLAS detector, Phys. Rev. D **90,** 052001 (2014).

[122] S. Chatrchyan *et al.* (CMS Collaboration), Search for Top Squarks in *R*-Parity-Violating Supersymmetry using Three or More Leptons and B-Tagged Jets, Phys. Rev. Lett. **111,** 221801 (2013).

[123] G. Aad *et al.* (ATLAS Collaboration), Search for massive supersymmetric particles decaying to many jets using the ATLAS detector in pp collisions at $\sqrt{s} = 8$ TeV, Phys. Rev. D **91,** 112016 (2015); , Erratum, Phys. Rev. D **93,** 039901 (2016).

[124] G. Aad *et al.* (ATLAS Collaboration), Search for super-symmetry at $\sqrt{s} = 8$ TeV in final states with jets and two same-sign leptons or three leptons with the ATLAS detector, J. High Energy Phys. 06 (2014) 035.

[125] S. Chatrchyan *et al.* (CMS Collaboration), Searches for light- and heavy-flavour three-jet resonances in pp colli-sions at $\sqrt{s} = 8$ TeV, Phys. Lett. B **730,** 193 (2014).

[126] S. Chatrchyan *et al.* (CMS Collaboration), Search for new physics in events with same-sign dileptons and jets in pp collisions at $\sqrt{s} = 8$ TeV, J. High Energy Phys. 01 (2014) 163; 01 (2015) 14.

[127] D. Dercks, H. Dreiner, M. E. Krauss, T. Opferkuch, and A. Reinert, R-parity violation at the LHC, Eur. Phys. J. C **77,** 856 (2017).

[128] B. Bhattacherjee and A. Chakraborty, Study of the bar-yonic *R*-parity violating MSSM using the jet substructure technique at the 14 TeV LHC, Phys. Rev. D **89,** 115016 (2014).

[129] J. Li, T. Li, and W. Zhang, Least constrained supersym-metry with *R*-parity violation, Phys. Rev. D **99,** 036011 (2019).

[130] G. Aad *et al.* (ATLAS Collaboration), Search for squarks and gluinos with the ATLAS detector in final states with jets and missing transverse momentum using $\sqrt{s} = 8$ TeV proton–proton collision data, J. High Energy Phys. 09 (2014) 176.

[131] CMS Collaboration, Search for supersymmetry in pp collisions at $\sqrt{s} = 8$ TeV in events with a single lepton, large jet multiplicity, and multiple b jets, Phys. Lett. B **733,** 328 (2013).

[132] CMS Collaboration, A search for scalar top quark pro-duction and decay to all hadronic final states in pp collisions at sqrt(s) = 8 TeV, Technical Report No. CMS-PAS-SUS-13-023, CERN, Geneva, 2015, https://cds.cern.ch/record/2044441.

[133] H. K. Dreiner and G. G. Ross, R-parity violation at hadron colliders, Nucl. Phys. **B365,** 597 (1991).

[134] J. Goity and M. Sher, Bounds on $\Delta B = 1$ couplings in the supersymmetric Standard Model, Phys. Lett. B **346,** 69 (1995); , Erratum, Phys. Lett. B **385,** 500 (1996).

[135] F. Zwirner, Observable delta B = 2 transitions without nucleon decay in a minimal supersymmetric extension of the Standard Model, Phys. Lett. B **132,** 103 (1983).

[136] B. Allanach, A. Dedes, and H. K. Dreiner, Bounds on *R*-parity violating couplings at the weak scale and at the GUT scale, Phys. Rev. D **60,** 075014 (1999).

[137] G. Bhattacharyya, D. Choudhury, and K. Sridhar, New lep bounds on b-violating scalar couplings: R-parity violating supersymmetry or diquarks, Phys. Lett. B **355,** 193 (1995).

[138] G. Bhattacharyya, A Brief review of R-parity violating couplings, in *Workshop on Physics Beyond the Standard Model: Beyond the Desert: Accelerator and Nonacceler-ator Approaches* (1997), pp. 194–201.

[139] E. L. Berger, B. W. Harris, and Z. Sullivan, Single Top Squark Production via *R*-Parity Violating Supersymmetric Couplings in Hadron Collisions, Phys. Rev. Lett. **83,** 4472 (1999).

[140] P. Abreu *et al.* (DELPHI Collaboration), Search for R-parity violation with a anti-U anti-D anti-D coupling at x**(1/2) = 189- GeV, Phys. Lett. B **500,** 22 (2001).

[141] P. D. Acton *et al.* (OPAL Collaboration), Search for massive, unstable photinos that violate R-parity, Phys. Lett. B **313,** 333 (1993).

[142] G. Abbiendi *et al.* (OPAL Collaboration), Searches for R-parity violating decays of gauginos at 183-GeV at LEP, Eur. Phys. J. C **11,** 619 (1999).

[143] G. Abbiendi *et al.* (OPAL Collaboration), Tests of the standard model and constraints on new physics from measurements of fermion pair production at 189-GeV at LEP, Eur. Phys. J. C **13,** 553 (2000).

[144] G. Abbiendi *et al.* (OPAL Collaboration), Search for R-parity violating decays of scalar fermions at LEP, Eur. Phys. J. C **12,** 1 (2000).

[145] G. Abbiendi *et al.* (OPAL Collaboration), Search for R parity violating decays of scalar fermions at LEP, Eur. Phys. J. C **33,** 149 (2004).

[146] T. Stelzer and S. Willenbrock, Single top quark production via $q\bar{q} \to t\bar{b}$, Phys. Lett. B **357,** 125 (1995).

[147] A. Datta, J. M. Yang, B.-L. Young, and X. Zhang, *R*-parity violating supersymmetry effects and signals in single top production at the Tevatron, Phys. Rev. D **56,** 3107 (1997).

[148] R. J. Oakes, K. Whisnant, J. M. Yang, B.-L. Young, and X. Zhang, Single top quark production as a probe of R-parity violating SUSY at **pp** and $p\bar{p}$ colliders, Phys. Rev. D **57,** 534 (1998).

[149] P. Chiappetta, A. Deandrea, E. Nagy, S. Negroni, G. Polesello, and J. M. Virey, Single top production at the CERN LHC as a probe of *R*-parity violation, Phys. Rev. D **61,** 115008 (2000).

[150] G. Aad *et al.* (ATLAS Collaboration), Search for phenom-ena beyond the Standard Model in events with large *b*-jet multiplicity using the ATLAS detector at the LHC, arXiv:2010.01015.

[151] M. Aaboud *et al.* (ATLAS Collaboration), A search for pair-produced resonances in four-jet final states at $\sqrt{s} =$ 13 TeV with the ATLAS detector, Eur. Phys. J. C **78,** 250 (2018).

[152] A. M. Sirunyan *et al.* (CMS Collaboration), Search for pair-produced resonances decaying to quark pairs in proton-proton collisions at $\sqrt{s} = 13$ TeV, Phys. Rev. D **98,** 112014 (2018).

[153] ATLAS Collaboration, Prospects for searches for staus, charginos and neutralinos at the high luminosity LHC with

the ATLAS detector, Technical Report No. ATL-PHYS-PUB-2018-048, CERN, Geneva, 2018, https://cds.cern.ch/record/2651927.

[154] D. Alves (LHC New Physics Working Group Collaboration), Simplified models for LHC new physics searches, J. Phys. G **39**, 105005 (2012).

[155] T. Sjostrand, L. Lonnblad, and S. Mrenna, PYTHIA 6.2: Physics and manual, arXiv:hep-ph/0108264.

[156] T. Sjstrand, S. Ask, J. R. Christiansen, R. Corke, N. Desai, P. Ilten, S. Mrenna, S. Prestel, C. O. Rasmussen, and P. Z. Skands, An introduction to PYTHIA 8.2, Comput. Phys. Commun. **191**, 159 (2015).

[157] J. Alwall, R. Frederix, S. Frixione, V. Hirschi, F. Maltoni, O. Mattelaer, H. S. Shao, T. Stelzer, P. Torrielli, and M. Zaro, The automated computation of tree-level and next-to-leading order differential cross sections, and their matching to parton shower simulations, J. High Energy Phys. 07 (2014) 079.

[158] J. de Favereau, C. Delaere, P. Demin, A. Giammanco, V. Lematre, A. Mertens, and M. Selvaggi (DELPHES 3 Collaboration), DELPHES 3, A modular framework for fast simulation of a generic collider experiment, J. High Energy Phys. 02 (2014) 057.

[159] https://twiki.cern.ch/twiki/bin/view/LHCPhysics/SUSY-CrossSections14TeVn2x1wino#Sum_of_NLO_NLL_wino_like_102_and.

[160] B. Fuks, M. Klasen, D. R. Lamprea, and M. Rothering, Precision predictions for electroweak superpartner production at hadron colliders with Resummino, Eur. Phys. J. C **73**, 2480 (2013).

[161] M. Tanabashi *et al.* (Particle Data Group Collaboration), Review of particle physics, Phys. Rev. D **98**, 030001 (2018).

[162] D. R. Tovey, On measuring the masses of pair-produced semi-invisibly decaying particles at hadron colliders, J. High Energy Phys. 04 (2008) 034.

[163] G. Polesello and D. R. Tovey, Supersymmetric particle mass measurement with the boost-corrected contransverse mass, J. High Energy Phys. 03 (2010) 030.

[164] ATLAS Collaboration, Study of the double Higgs production channel $H(\to b\bar{b})H(\to \gamma\gamma)$ with the ATLAS experiment at the HL-LHC, Technical Report No. ATL-PHYS-PUB-2017-001, CERN, Geneva, 2017, http://cds.cern.ch/record/2243387.

[165] ATLAS Collaboration, Search for Supersymmetry at the high luminosity LHC with the ATLAS experiment, Technical Report No. ATL-PHYS-PUB-2014-010, CERN, Geneva, 2014, http://cds.cern.ch/record/1735031.

[166] W. Beenakker, R. Hopker, and M. Spira, PROSPINO: A Program for the production of supersymmetric particles in next-to-leading order QCD, arXiv:hep-ph/9611232.

[167] W. Beenakker, M. Klasen, M. Kramer, T. Plehn, M. Spira, and P. M. Zerwas, The Production of Charginos/Neutralinos and Sleptons at Hadron Colliders, Phys. Rev. Lett. **83**, 3780 (1999); , Erratum, Phys. Rev. Lett. **100**, 029901 (2008).

[168] A. Djouadi, M. M. Muhlleitner, and M. Spira, Decays of supersymmetric particles: The program SUSY-HIT (SUspect-SdecaY-Hdecay-InTerface), Acta Phys. Pol. B **38**, 635 (2007).